Seismic properties across an amphibolite- to greenschist-facies strain gradient (Neves area, eastern Alps, Italy): New considerations for shear zone imaging

Thomas Leydier, Philippe Goncalves, Julie Albaric, Henri Leclère, Kevin Mahan, Daniel Faulkner

Seismic properties across an amphibolite- to greenschist-facies strain gradient (Neves area, eastern Alps, Italy): new considerations for shear zone imaging

Thomas Leydier[a,*], Philippe Goncalves[a], Julie Albaric[a], Henri Leclère[a], Kevin H. Mahan[b], Daniel Faulkner[c]

[a] *Université de Bourgogne Franche-Comté – UMR-CNRS 6249 Laboratoire Chrono-Environnement, 16 route de Gray 25000 Besancon, FR*
[b] *Department of Geological Sciences, University of Colorado Boulder, 2200 Colorado Ave, Boulder, Colorado 80309*
[c] *Department of Earth and Ocean Sciences, University of Liverpool, 4 Brownlow Street, Liverpool, L69 3GP, UK*

Keywords: *Seismic anisotropy, shear zone, EBSD, ultrasonic measurements*

Highlights :

1. Non-linear evolution of P- and S- wave anisotropy with ductile strain
2. Unexpected anisotropy destruction in mylonite due to a change in mica texture
3. Magnitude and geometry of seismic anisotropy controlled by metamorphic conditions
4. Bulk shear zone seismic properties controlled by the S plane-dominated margins

ABSTRACT

Detecting the presence and geometry of crustal shear zones by geophysical methods relies on our understanding of the intrinsic parameters controlling the seismic properties of these deformed rocks, over the range of pressure-temperature conditions expected in the Earth's crust. To this end, we aimed to track changes in P-wave propagation velocity (V_P), anisotropy (AV_P) and S-wave splitting (AV_S) across a natural shear zone using experimental and electron backscatter diffraction methods. Five samples were collected across a meter-scale shear zone developed under amphibolite- to greenschist-facies in the Neves metagranodiorite (Tauern Window, Eastern Alps). With increasing strain, seismic properties show a non-linear evolution resulting from interactions among structural, textural and mineralogical changes. Geometry and magnitude of seismic anisotropy are controlled by the interference

*Corresponding author.
E-mail adress: **thomas.leydier@umontpellier.fr** *Tel:* **+33649899575**
Present address: Géosciences Montpellier, UMR CNRS 5243, Université de Montpellier, Montpellier, France

of strongly anisotropic phyllosilicates with less anisotropic but more abundant quartz and plagioclase. The amphibolite-facies shear zone margin (> 500°C) is free of major mineral transformations, and rather characterized by the development of S-C structure, inducing an orthorhombic symmetry to the V_P distribution and up to 12 % AVP, with the fast axis parallel to lineation. AV_S is maximized (6 %) in the two directions parallel to the C-planes. Further deformation under greenschist-facies (450-500°C) induces significant crystallization of muscovite, chlorite, and albite. A dominant hexagonal symmetry develops, with a fast VP plane and a fast S-wave polarization plane along the C-planes. AV_P and AV_S exceed 10 %. The computed elastic tensor of the whole shear zone emphasizes the importance of the strain gradient on the seismic signature of the overall structure. In our model, the bulk seismic properties are dominated by the orthorhombic symmetry of the protomylonitic zone rather than by the ultramylonite core with hexagonal symmetry (C-plane), which may explain why seismic studies of shear zones commonly involve a fast velocity plane oblique to the layer boundaries.

1. Introduction

Characterizing the structure and the geometry of shear zones is crucial for better understanding the overall behavior of the Earth's lithosphere. Indeed, one of the main challenges in geosciences is to improve our knowledge of the interactions between the different layers of the lithosphere, and shear zones play a key role in these interactions since they constitute the deep roots of transcrustal discontinuities (e.g. Sibson, 1977). Involving both brittle and ductile deformation mechanisms (e.g. Hayman and Lavier, 2014; Segall and Simpson, 1986) and acting as fluid channels allowing important chemical mass transfer (e.g. Goncalves et al., 2012; Oliot et al., 2010), they thus make a chemical and rheological link between the processes operating in the shallower crust and in the lithospheric mantle. The vertical link with the seismogenic upper crust is also crucial to investigate, since shear zones can host brittle-ductile cyclic processes that still have poorly understood roles in the overall seismic cycle (e.g. Hayman and Lavier, 2014; Fusseis and Handy, 2008). However, imaging these highly deformed systems with sufficient resolution is still challenging. Among geophysical techniques, receiver functions (RF) have been successful in detecting velocity contrasts and anisotropic domains

highlighting the presence of deep crustal shear zones (e.g. Phinney, 1964; Burdick and Langston, 1977; Schulte-Pelkum and Mahan, 2014). One of the limitations of these methods is due to the use of simplified geological models for shear zones consisting of homogeneous anisotropic fabrics surrounded by isotropic protoliths (e.g. Schulte-Pelkum et al., 2005), while the relationship between strain and seismic properties within shear zones is made more complex by the variety of intrinsic parameters (mineralogy, crystal preferred orientation, structure). For example, Schulte-Pelkum et al. (2005) used RFs to image a crustal decollement beneath the Himalaya and quantified an angle of $\sim$40° between the inferred anisotropic foliation and the expected dip of the shear zone boundaries. This suggests that the seismic anisotropy is not solely controlled by the highest strained part of the shear zone, where the ultramylonitic foliation is presumed to be parallel to the shear zone boundaries. Other parameters must thus be considered for explaining some seismically anisotropic crustal-scale shear zones that may have more heterogeneous geometries (e.g. Fossen and Cavalcante, 2017; Fusseis et al., 2006).

In this paper, we propose an improved geological model to be considered for geophysical investigations of shear zones. A mineralogical and microtextural analysis is combined with the quantification of seismic properties on an exposed meter-scale Alpine shear zone from the Tauern Window in Eastern Alps (Neves area, Tyrol, Italy). Along the ductile strain gradient, a suite of 5 samples were collected with various degree of deformation (from the protolith to the ultramylonitic core). Seismic properties of each sample were quantified by the means of two independent methods: (1) laboratory measurements of elastic wave velocities on cylindrical samples (P wave velocity V_P, P wave anisotropy AV_P and shear wave splitting AV_S) and (2) calculation of the bulk elastic properties of the full polycrystalline aggregate and wave velocities from crystal orientation mesaurements derived from electron backscatter diffraction (EBSD) (Mainprice, 2007). Estimation of deformed rocks' seismic properties by the experimental (e.g. Barruol et al., 1992; Jones and Nur, 1982; Leclère et al., 2015; Wenning et al., 2016) or numerical methods (e.g. Punturo et al., 2014; Tatham et al., 2008) has previously been performed, mostly focusing on P wave anisotropy. However, they have rarely been compared with each other. P and S wave velocity estimated in mylonites are about 6.0±1.0 and 3.5±0.5 $km.s^{-1}$, respectively, and

always lower when the propagation direction is normal to the foliation (e.g. Chroston and Max, 1988; Wenning et al., 2016). AV_P and AV_S in mylonites have been estimated at 8-11 % (e.g. Fountain, 1976; Jones and Nur, 1982) and 6-7 %, respectively (e.g. Ji and Salisbury, 1993). AV_S is usually lower when the propagation direction is normal to the foliation (e.g. Barruol et al., 1992; Ji and Salisbury, 1993). Although the modal proportion and fabrics of micas are generally assumed as the main source of seismic anisotropy in mylonites, the role of other constituting phases of the lower crust, like amphibole, has also been highlighted (Tatham et al., 2008).

Although these two methods have been widely used independently, their application together on the same natural samples is less common. In this work, the combination of both methods is used to quantify the relative contributions of structure, texture and crystal preferred orientation and mineralogy on the seismic properties of shear zones (e.g. Almqvist et al., 2013; Barruol et al., 1992). Particular attention is paid to the interferences between the strongly anisotropic phase (e.g. phyllosilicates) and less anisotropic but more abundant rock-forming phases like quartz and plagioclase. Calculated bulk elastic stiffnesses and wave velocities of each sample are combined, re-oriented and weighted to elucidate the seismic behavior of a theoretical shear zone consisting of a protolith, an intermediate zone with a foliation at high angle to the shear plane, and a high strain core oriented parallel to the shear plane. This analysis is used to discuss the overall strength and geometry of seismic anisotropy generated by a crustal shear zone, and to add a geological constrain to the initial models used to predict their geophysical signature.

2. Geological context and sampling strategy

Within the austroalpine Eastern Alps, the Tauern Window exposes Variscan continental basement intruded by a late-Variscan batholith, the Zentralgneise (Fig.1a; e.g. Morteani, 1974; Schmid et al., 2013). This complex was buried and deformed during the Alpine orogeny (c. 28-30 Ma), reaching peak conditions of 550-600°C and 0.5-0.7 GPa, corresponding to amphibolite-facies metamorphism (e.g. Christensen et al., 1994). The Variscan metasediments were pervasively mylonitized, while the more resistant magmatic intrusions were only weakly affected by deformation (e.g. Morteani, 1974;

Glodny et al., 2008). Thus today, the Tauern Window shows a structural pattern that is typical of the ductile deformation of granitic regions (e.g. Choukroune and Gapais, 1983), which is inherited from these rheological heterogeneities. It is characterized by an anastomozing geometry defined by low-strain granodioritic domains surrounded by km-scale mylonitized Variscan metasediments. Only the low-strain granodioritic domains embedded in this crustal-scale shear zone system preserve the m-scale strain gradients that are of interest for our analysis.

The study area is located in the south-western part of the Zentralgneise, 4 km northeast of Neves lake (South Tyrol, Italy). It is a glacier-polished region of nearly 500 000 m^2, exposed by the retreat of the Mesule glacier (Fig.1b). It has been described in detail by Mancktelow and Pennacchioni (2005) and Pennacchioni and Mancktelow (2007). The dominant lithology is a late-Variscan metagranodiorite, affected by many magmatic dykes. In the core of the low-strain domain, alpine deformation occurs as localized cm- to m-wide shear zones. The shear zones localized on viscosity contrasts, such as the margins of aplite dykes or brittle fractures, affecting the metagranodiorite. The studied outcrop is a steeply dipping, dextral alpine shear zone of nearly 2 m in width, oriented east-west (Fig.1c). In order to study the role of ductile strain localization on the seismic properties, 4 homogeneously deformed samples were collected from the shear zone, corresponding to 4 successive deformation stages: protomylonite 1 (18NEV01A), protomylonite 2 (18NEV01B), mylonite (13NEV01C) and ultramylonite (13NEV01D) (Fig.1d). As a reference frame, one sample was collected in the surrounding undeformed protolith (13NEV01A), which preserves an inherited magmatic north-south fabric at high angle to the shear zone and allows us to investigate the role of the protolith fabric on the anisotropy of the whole shear zone.

3. Methods

3.1. Elastic-wave velocity measurements

Velocity measurements of ultrasonic waves (P and S) were performed in a high-pressure hydrostatic apparatus ($\sigma_1 = \sigma_2 = \sigma_3$) located in the Rock Deformation Laboratory at the University of Liverpool

(UK) (Armitage et al., 2011; Blake et al., 2013). The apparatus uses low-viscosity silicon oil (10 cS) as the confining medium and is equipped with an ultrasonic active acquisition system. Experiments were carried out in room-dry conditions and at room temperature on cores of 20 mm in diameter and between 20 and 90 mm in length. Cores of the ultramylonite could not be recovered from the field samples due to the friable nature of the material. Cores were squared and then placed in a 3-mm thick PVC jacket to prevent infiltration of the confining silicon oil into the samples. Velocity measurements were conducted at 250 MPa, which is the maximum confining pressure supported by the apparatus. At these conditions, we expect to close most of the open microcracks and measure the intrinsic seismic properties of mineral aggregates (see section 4.3). Indeed, many experimental studies have described an asymptotic evolution of seismic properties with increasing confining pressure, consisting in a fast, non linear velocity increase (and anisotropy decrease) at lower pressure, followed by a more progressive, linear evolution (e.g. Birch, 1960; Christensen, 1965; Kern and Wenk, 1990; Blake et al., 2013). This behavior has been interpreted as the closure of most of the open microcracks, until a crack-closing pressure that ranges from 100 to 250 MPa (e.g. Christensen, 1965; Kern and Wenk, 1990)). It is also noteworthy that at high confining pressure, the signal-to-noise ratio is maximized, thus reducing uncertainties in arrival time picking.

Jacketed cores were clamped between the top and the bottom loading platens on which P and S 1-MHz piezoelectric ceramic transducers are glued. P- or S-seismic waves are emitted from the bottom platen with P_{bottom} and S_{bottom} transducers and recorded by P- and S-top transducers. The top S-tranducer records on two components, S_1 and S_2, which are at 90° from each other, and point toward East and North, respectively in the (N, E, d) coordinate system depicted in Supplementary Material S1. The S_{bottom} emitting transducer is polarized N45°E and P_{bottom} is vertical. This source-receiver geometry allows the recording of P- and S-wave velocity, as well as shear-wave splitting (see Supplementary Material S2 for the pulser-receiver settings, after Blake, 2011). Cores were oriented in the sample assembly according to the orientation of the foliation or the lineation which are aligned with S_1 (Supplementary Material S1).

Data acquisition was performed using the pulse-transmission technique and by averaging 512 stacked signals, to optimize the signal-to-noise ratio (see Supplementary Material S3a-d). Seismic velocities are calculated by picking the first seismic phase arrival time (see Supplementary Material S3e). Picking error is estimated with the method of Diehl et al. (2009), in which the arrival (a) of the seismic phase is considered as a probabilistic function $P_a(t)$. The arrival time (t_A) is expressed as the most likely arrival time ($P_a(t) = (max)P_a$), included in a temporal uncertainty window defined by the earliest (t_E) and the latest (t_L) arrival times, where P_a tends to zero. t_E and t_L are defined using the Amplitude-based Signal-to-Noise Ratio (ASNR). The error increases as the interval between t_E and t_L increases. Velocity anisotropy is calculated as follows (e.g. Birch, 1960; Mainprice and Humbert, 1994) :

$$A(\%) = 200 \times \frac{(V_{max} - V_{min})}{(V_{max} + V_{min})} \quad (1)$$

AV_P is inferred from the maximum and minimum velocity among the V_P measured along the X-, Y- and Z- cores of each rock sample. AV_S is estimated for each core, from the maximum and minimum velocity among V_{S1} and V_{S2}.

3.2. Calculating rock aggregate seismic properties from petrofabrics

Crystallographic preferred orientations (CPO) were measured using electron backscatter diffraction (EBSD) with a Hitachi SU3500 scanning electron microscope equipped with a W source electron gun at the University of Colorado Boulder (USA). Analytical settings are summarized in the Supplementary Material S4. CPOs are plotted in the structural reference frame of the sample, where X-, Y- and Z-axes correspond to the three principal directions of the strain ellipsoid. Fabric strength is expressed with the J index (Bunge and Esling, 1982). The J index has a value of one for random orientations and scales infinitely with increasing texture strength, although typical "high" values for natural polycrystals range from 10 to 100. Indexing phyllosilicates by EBSD is very challenging (Prior et al., 2009). EBSD data acquired on micas is biased by the dependence of their indexing rate on their crystallographic orientation: mica indexing is higher on the basal (001) plane. To avoid the overestimation of

this population, we selected regions of interest where the relative proportion of the underestimated population (basal plane at high angle to the thin section) is sufficient to balance the better indexing of the first one (see Supplementary Material S5). It results in a more representative overall fabric. Calculations of elastic tensor and seismic velocities of polymineralic aggregates (Mainprice and Casey, 1990; Mainprice and Humbert, 1994) are based on the volume fraction, CPO and the elastic tensor of each mineral phase, from Ogi et al. (2006) (quartz), Brown et al. (2016) (plagioclase), Waeselmann et al. (2016) (K-feldspar), Vaughan and Guggenheim (1986) (muscovite), Aleksandrov and TV (1961) (biotite and chlorite); Ryzhova et al. (1966) (epidote) and Jiang et al. (2004) (garnet). Single crystal elastic tensors are rotated according to their CPO and then weighted according to their modal proportions. Seismic properties of the rock aggregate are calculated using the Voigt-Reuss-Hill average (VRH; Hill, 1952), which is the arithmetic mean of the Voigt (iso-strain boundary; Voigt, 1928) and Reuss (iso-stress boundary; Reuss, 1929) approximations. The VRH approximation is widely used to estimate the elastic properties of anisotropic polycrystalline aggregates since it provides consistent values with laboratory measurements of seismic velocities (e.g., Mainprice and Humbert, 1994; Bunge et al., 2000). Seismic properties are calculated with the MATLAB software toolbox MTEX, developed by D. Mainprice (Mainprice, 1990; Mainprice et al., 2011; Hielscher and Schaeben, 2008).

4. Results

4.1. Structural and mineralogical evolution

The magmatic assemblage of the Neves metagranodiorite consists of plagioclase (48 vol %), quartz (28 vol.%), biotite (14 vol.%) and minor K-feldspar (9 vol.%) (Fig.2a-b). Igneous plagioclase (Pl_0), occurs as coarse ($\sim$ 1 mm) subhedral grains, and is saussuritized, i.e. altered to a more Na-rich plagioclase containing a fine-grained assemblage of white mica and epidote (1 vol.%). These inclusions measure from a few tens to a few hundreds of μm and are randomly oriented within the host crystal (Fig.2c). Quartz occurs as aggregates of large grains of 500 μm to 1 mm in size, with irregular, serrate-to-lobate boundaries. Quartz grains are affected by weak intracystalline deformation revealed

by discrete undulose extinction and rare recrystallized bands (Fig.2c). K-feldspar occurs as a late-crystallized interstitial phase in plagioclase-rich domains (Fig.2b). Igneous biotite (Bt_0) is surrounded by recrystallized fine-grain metamorphic biotite (Bt_1) (Fig.2d). Magmatic plagioclase and biotite define a weak magmatic foliation that trends north-south (Fig.2a).

Protomylonitic deformation is characterized by the development of a C-S-C' fabric, as observed in protomylonite 2 (Fig.3a). The intermediate stage protomylonite 1 shows similar but less-developped features, and will not be extensively described here (see Supplementary Material S6). Quartz-rich domains (26 vol.%) form recrystallized aggregates with an elongated, assymetrical sigmoidal shape, with preferred stretching parallel to C, consistent with dextral shearing (Fig.3a). These aggregates are recrystallized to grains with a size of a few hundred μm, showing interlobate boundaries (Fig.21b), suggesting that deformation occurred via dislocation creep accommodated by grain boundary migration (GBM, Guillope and Poirier, 1979; Urai et al., 1986; Stipp et al., 2002). Quartz <c> axes show three maxima between Z- and Y-axes (J=3.8), which is consistent with a basal <a> slip system assisted by the understated intervention of prismatic <a> slip (Fig.3c, e.g. Mainprice et al., 1986; Stipp et al., 2002). Plagioclase occurs as a fine-grained recrystallized matrix in which the grain size does not exceed 100 μm (Fig.3a). These recrystallized plagioclase aggregates form elongated interconnected weak layers surrounding coarse quartz lenses. Saussuritized plagioclase phenocrysts, described in the protolith, are lacking. All these observations suggest that during the onset of strain localization, plagioclase is likely to have been the weakest phase. Although recrystallized plagioclase shows scattered crystallographic orientations (J=1.9), poles (010) and (100) define a diffuse maxima at low angle to the X- and Z-axes, respectively (Fig.3c), consistent with a (100)<010> slip system. Interconnected thin layers of biotite (13 vol.%) and to a lesser extent muscovite (5 vol.%), define sigmoidal lenses within the plagioclase matrix and outline the quartz lenses boundaries (Fig.3a). They also highlight the development of a secondary shear plane C', that was not present in protomylonite 1, where biotite remained scattered and did not form interconnected ribbons yet (see Supplementary Material S6). A few grains of Bt_0 are preserved as porphyroclasts with cleavage at high angle to the foliation planes (Fig.3a), likely

at the origin of the diffuse maxima of <c> axes in the center of the pole figure (Fig.3c). Biotite shows the strongest fabric (J=19.1), which is due in part to the weaker contribution from this diffuse intermediate maxima corresponding to magmatic fabrics (Fig.3c), with respect to protomylonite 1 (see Supplementary Material S6). Neo-crystallization of metamorphic muscovite is observed and is likely related to K-feldspar breakdown (2 vol.%).

Mylonite 13NEV01C (Fig.4) is characterized by the development of a gneissic layering parallel to the shear plane. It consists of mm-thick quartz ribbons (33 vol.%) interlayered with plagioclase- (46 vol.%), epidote- (7 vol.%) and mica-rich (13 vol.%) domains (Fig.4a). The plagioclase matrix is very fine-grained (Fig.4a,b) with a weak CPO (J=1.4). A dominant slip system is now very difficult to infer from the CPO (Fig.4d). Recrystallized quartz (Fig.4b) has a smaller grain size than in the protomylonites (40-500 μm). All quartz grains show evidence for very mobile grain boundaries (GBM). Quartz grains are elongated with a shape-preferred orientation (SPO) at $\sim$35° to the C-planes, consistent with dextral shearing (Fig.4b). Quartz <c> axes still show maxima at low angle from Z, indicating basal <a> dextral slip (Fig.4d, Mainprice et al., 1986). There is no evidence for prismatic slip. We observe a decrease of the biotite modal proportion (9 vol.%) and fabric strength (J=6.4). The diffuse maximum of the <c> axes close to the Y axis cannot be explained by the presence of magmatic relicts, since they completely recrystallized (Fig.4d). Biotite and muscovite (4 vol.%) ribbons delimit the epidote-rich plagioclase matrix from the quartz domains (Fig.4c).

Ultramylonite 13NEV01D (Fig.5) shows a significant change in mineralogy, with the complete breakdown of biotite (<1 vol.%), epidote, garnet and K-feldspar, the production of a more albite-rich plagioclase, the crystallization of muscovite (21 vol.%) and, to a lesser extent, chlorite (3 vol.%). Muscovite and chlorite occur as ribbons defining a very narrow foliation ($\sim$500 μm, Fig.5a,b). Plagioclase is less abundant than in the less deformed rocks (30 vol.%). Cathodoluminescence imaging of plagioclase (Fig.5c) shows two distinct populations, based on the Na/Ca ratio : a Ca-richer population (oligoclase, green in CL) and a Na-richer one (albite, red in CL). The two populations of plagioclase show a weak CPO, with the (100) planes parallel to the foliation. Oligoclase does not show any clear slip direction,

but albite (010) poles are close to the lineation, suggesting a (100)<010> slip system (Fig.5d). Quartz (43 vol.%) occurs as either thin recrystallized ribbons or mixed with plagioclase. Grain size ranges from 40 to 100 μm, while the largest quartz grains can reach 250 μm (Fig.5b). Quartz fabric is weak (J=1.8) compared to less deformed rocks and the <c> axes form a girdle between the two poles of the foliation, with a maximum located between the Z- and Y-axes (Fig.5d). We suggest that quartz in the ultramylonite deformed mostly via the rhomb <a> slip system (e.g. Mainprice et al., 1986).

4.2. Pressure-temperature conditions of deformation

The main mineralogical change described along the strain gradient occurs between the mylonite and the ultramylonite and consists of the breakdown of biotite and plagioclase to produce muscovite, albite and chlorite. To constrain the P-T conditions of this transition, phase relations were modeled. The phase diagram shown in Fig.6 is derived from a pseudosection (isochemical phase diagram) computed with the bulk composition of the ultramylonite, in the H2O saturated Na2O–CaO–K2O–FeO–MgO–Al2O3–SiO2 system with *Perple*$_X$ 6.8.8 (Connolly and Kerrick, 1987; Connolly, 2005). This phase diagram shows an univariant equilibrium Pl + Kf + Bt + Qz + H2O = Mu + Chl + Ab + Ep at ~450-475°C. For the selected bulk composition, four divariant equilibria are stable over the P-T space associated with the above equilibrium (white fields in Fig. 6). Among them, those located on the high pressure side (Chl) and (Kf) are relevant for the studied sample. Along a cooling path, the (Chl) divariant equilibrium is responsible for the breakdown of the high temperature assemblage Pl Kf Bt Ep Qz into a Bt Mu Ep Ab Pl Qz assemblage. With further cooling, the divariant (Kf) equilibrium is crossed and the assemblage Pl + Bt is broken down to produce the Mu Chl Ab-bearing assemblage that is characteristic of the ultramylonite. This phase relation modeling shows that the development of the meter-wide strain gradient occurred during a cooling path from ~500 to ~475°C at a pressure greater than 0.5-0.6 GPa. The high-temperature portion of this cooling path is consistent with the thermal peak of the "Tauern metamorphism", and to the amphibolite-facies conditions of deformation inferred from mineralogy and quartz deformation mechanisms by previous metamorphic studies (e.g. Christensen et al., 1994; Mancktelow and Pennacchioni, 2005).

The evolution of mineralogy, microtexture and metamorphic conditions are summarized in Fig.7. Modal proportions are inferred from the combination of the EBSD data, scanning electron microscopy and cathodoluminescence imaging. In the following, the strain gradient will be divided in three parts: (1) the undeformed, metastable protolith bearing an inherited magmatic foliation, (2) the amphibolite-facies margin of the shear zone, consisting of protomylonite 1, protomylonite 2 and mylonite, characterized by a stable mineralogy and a widespread recrystallization, and (3) the greenschist-facies high-strain core of the shear zone, the ultramylonite, marked by the important crystallization of muscovite, chlorite and albite. It reflects the evolution of the P-T conditions during the formation of the shear zone, which started under amphibolite-facies conditions and continued under retrograde conditions related to the exhumation episode, recorded in the greenschist-facies assemblage in the core of the shear zone.

4.3. Measured seismic properties

Measured and calculated seismic properties along the strain gradient are summarized in Table 1.

Figure 8 shows the evolution of the measured V_P (Fig.8a), AV_P (Fig.8b), and AV_S (Fig.8c) with strain, from the protolith to the mylonite. In the protolith, V_P ranges from 5.97±0.9 to 6.25 ±0.08 $km.s^{-1}$, which corresponds to 4.6±0.3 % of P-wave anisotropy. In one of the three measured cores, S-wave anisotropy reaches a maximum value of 5.9 ±1.6 %. The three perpendicular cores of the protolith are not oriented with respect to a reference frame, therefore the AV_P and AV_S values should not be treated as maximum values. In any case, the protolith already presents seismic anisotropy.

In the amphibolite-facies shear zone, from protomylonite 1 to mylonite, seismic P-wave velocities are not significantly different with respect to the protolith (Fig.8a). In all samples, the fast P-wave propagation direction is always parallel to the lineation direction (X-axis) and ranges from $V_P(X)$ = 6.22 ±0.09 to 6.44 ±0.14 $km.s^{-1}$. In contrast, P-waves propagating normal to the foliation and shear planes (Z-axis) are systematically the slowest and do not vary significantly with strain ($V_P(Z)$ = 5.70 ±0.08 to 5.90 ±0.25 $km.s^{-1}$). In the protomylonites, P-waves propagating along the Y-axis have an

Table 1: Measured and calculated seismic properties across the Neves meter-scale strain gradient.

	Measured seismic properties			**Calculated seismic properties**			
Protolith	*C1*	*C2*	*C3*	*C1*	*C2*		*C3*
V_P $(km.s^{-1})$	6.25±0.08	6.11±0.04	5.97±0.9	6.41	6.20		6.25
AV_P (%)		4.6±0.3				4.6	
V_{S1} $(km.s^{-1})$	3.41±0.14	3.40±0.26	3.47±0.16	3.73	3.70		3.74
V_{S2} $(km.s^{-1})$	3.41±0.15	3.32±0.17	3.68±0.33	3.58	3.58		3.70
AV_S (%)	0.0	2.4±0.6	5.9±1.6	4.1	3.3		1.1
Protomylonite 1	*X*	*Y*	*Z*	*X*	*Y*		*Z*
V_P $(km.s^{-1})$	6.34±0.04	6.19±0.12	5.80±0.41	6.80	6.64		6.50
AV_P (%)		8.9±1.4				5.2	
V_{S1} $(km.s^{-1})$	3.78±0.15	3.77±0.25	3.24±0.35	4.08	4.08		4.00
V_{S2} $(km.s^{-1})$	3.65±0.13	3.65±0.39	3.28±0.27	3.98	3.98		3.92
AV_S (%)	3.5±0.5	3.3±1.1	1.2±0.5	2.48	4.00		2.02
Protomylonite 2	*X*	*Y*	*Z*	*X*	*Y*		*Z*
V_P $(km.s^{-1})$	6.44±0.14	6.14±0.17	5.70±0.08	6.80	6.65		6.42
AV_P (%)		12.2±0.9				7.3	
V_{S1} $(km.s^{-1})$	3.79±0.29	3.90±0.40	3.35±0.18	4.05	4.05		3.88
V_{S2} $(km.s^{-1})$	3.55±0.16	3.63±0.32	3.36±0.17	3.85	3.80		3.80
AV_S (%)	6.6±1.6	7.0±2.8	0.5±0.1	5.06	6.37		2.08
Mylonite	*X*	*Y*	*Z*	*X*	*Y*		*Z*
V_P $(km.s^{-1})$	6.22±0.09	6.24±0.08	5.90±0.25	6.90	6.69		6.67
AV_P (%)		5.6±0.6				4.7	
V_{S1} $(km.s^{-1})$	3.82±0.25	3.78±0.32	3.34±0.59	4.14	4.12		4.09
V_{S2} $(km.s^{-1})$	3.69±0.17	3.57±0.34	3.34±0.53	4.07	4.02		4.01
AV_S (%)	3.6±0.8	5.6±2.0	0.3±0.2	1.70	2.47		1.98
Ultramylonite	*X*	*Y*	*Z*	*X*	*Y*		*Z*
V_P $(km.s^{-1})$	-	-	-	6.60	6.60		6.0
AV_P (%)		-				10.6	
V_{S1} $(km.s^{-1})$	-	-	-	4.02	4.02		3.72
V_{S2} $(km.s^{-1})$	-	-	-	3.74	3.74		3.64
AV_S (%)	-	-	-	7.22	7.22		0.54

intermediate velocity leading to an orthorhombic symmetry ($X \neq Y \neq Z$) for velocity anisotropy. In the mylonite, $V_P(X)$ decreases down to 6.22 $\pm$0.09 $km.s^{-1}$ such that $V_P(X) = V_P(Y)$. Thus, the symmetry of the velocity distribution in the mylonite is hexagonal ($X = Y \neq Z$) with a slow symmetry axis corresponding to the Z axis. The magnitude of velocity anisotropy shows large variations with strain (Fig.8b).

In the protomylonite, AV_P increases significantly and reaches 12.2 $\pm$0.9 % in protomylonite 2. The mylonite is characterized by a decrease of anisotropy with an unexpected low AV_P = 5.6 $\pm$0.6 %, comparable to the undeformed protolith. Shear wave splitting is almost null along the Z-axis (AV_S < 1.2 $\pm$0.5 %). In contrast, shear wave anisotropy is maximum when S wave-propagation direction is parallel to the foliation or shear plane. The lineation does not influence shear wave anisotropy (i.e. $AV_S(X) = AV_S(Y)$). Similar to AV_P, AV_S is at its maximum in protomylonite 2 (6.6 $\pm$1.6 % and 7.0 $\pm$2.8 % along X- and Y-axes, respectively), then it decreases to ca. 3 to 4 % in the mylonite.

4.4. Calculated seismic properties

4.4.1. Aggregate seismic properties

Figures 9 to 12 show for each sample of the strain gradient: (a) the modal abundance of each phase, (b) the CPO of the crystallographic direction corresponding to the fast, intermediate and slow P-wave propagation directions for each phase, (c) the seismic properties (V_P distribution, AV_P, and AV_S distribution) computed for each phase and, finally, (d) the seismic properties of the whole rock aggregate. The location of EBSD maps is showed in the Supplementary Material S7. The results for protomylonite 1 are shown in the Supplementary Material S8. The stereographic projections showing the computed distributions of V_{S1} and V_{S2} are available in the Supplementary Material S9. The bulk elastic tensors calculated for each sample are summarized in the Supplementary Material S10.

Protolith

In the protolith (Fig.9), the distribution of V_P is mainly controlled by plagioclase (AV_P(Plagioclase) = 6 %), which represents 48 % of the rock volume (Fig.9a), and more particularly by the orientation of its fast direction (010) normal to the twin planes, and thus to the magmatic foliation (Fig.9b). Although

biotite has the highest single phase AV_P (9.7 %), the low modal abundance (14 %) combined with lack of preferred crystallographic orientation means that it exerts little systematic control on the bulk V_P distribution and AV_P (Fig.9c). Due to its weak seismic anisotropy, quartz does not contribute to increase that of the aggregate. As a result of plagioclase and biotite contributions, the fastest P-wave velocities ($\sim$6.3 $km.s^{-1}$) of the aggregate are concentrated at high angles to the magmatic foliation with a bulk AV_P of 4.6 % (Fig.9d). AV_S locally reaches 4.5 % but, in contrast to V_P, these maxima do not show any link with the igneous structure.

Amphibolite-facies shear zone: protomylonites and mylonite

The calculated V_P of the two protomylonites and mylonite, belonging to the amphibolite-facies strain gradient, are higher than that of the protolith and range from 6.4 to 7.0 $km.s^{-1}$ (Fig.10,11, see Supplementary Material S8 for protomylonite 1). The V_P anisotropy of the protomylonites and mylonite have an orthorhombic symmetry with the fast propagation axis parallel to lineation (X) and the slow propagation axis normal to the foliation (Z) (Fig.10d). AV_P for the aggregate increases with strain and reaches a maximum value of 7.3 % in protomylonite 2 (Fig.10d). In the mylonite, AV_P decreases to 4.7 % (Fig.11d). The absolute values and the distribution of AV_S show the same evolution with strain. In the protomylonites, AV_S is maximum when the S-wave propagates within the foliation plane. There is almost no splitting perpendicular to the foliation plane ($AV_S < 2$ %). The maximum value of AV_S reaches 6.5 % in protomylonite 2 and decreases to 4.0 % in the mylonite. The distribution of AV_S in the mylonite is complex without any clear relationship with the strain ellipsoid.

The anisotropy of wave speeds in protomylonite and mylonite samples directly reflect the behavior of phyllosilicates. Biotite and muscovite represent almost 20 % of the rock volume in the protomylonites and show the highest values of seismic anisotropy for both P- (38.7 and 40.3 % for biotite and muscovite respectively in protomylonite 2) and S-waves (up to 40 %, Fig.10c).

While in protomylonite 1, biotite fabric was influenced by the presence of magmatic relicts oriented at high angle to the shear plane (see Supplementary Materials S6 and S8), magmatic biotite is less abundant in protomylonite 2, leading to a strong fabric strength (J index = 19 for biotite, Fig.10b).

This evolution in phyllosilicate fabric strength is likely responsible for the progressive transition from orthorhombic to hexagonal symmetry of the whole aggregate and the increase in the magnitude of the seismic anisotropy .

The weakening of seismic anisotropy magnitude in the mylonite ($AV_P = 4.7$ % and $AV_S < 4$ %) is due to (1) a decrease in the modal proportion of mica (from 18 to 13 %, Fig.11a) and to (2) a decrease in fabric strength of mica (J index < 6.5 and 4 for biotite and muscovite, Fig.11b) due to a relatively large number of grains with their slow c-axes parallel to Y, in addition to metamorphic phyllosilicates parallel to the foliation plane (slow c-axis parallel to Z). As in the protomylonite, biotite oriented at high angles to the foliation plane is likely due to magmatic relicts. However, muscovite oriented at such high angles to the foliation plane cannot be magmatic since muscovite is essentially metamorphic and well-parallelized to the foliation. We speculate that these muscovite data are misindexed magmatic biotite.

Although plagioclase and quartz have a much weaker CPO and seismic anisotropy (AV_P and $AV_S < 5$ %), their large modal abundance (∼75 % together) counteracts and attenuates the effect of the phyllosilicates on the bulk seismic properties. Because the fast propagation axis of plagioclase (010) is nearly parallel to the lineation, it contributes in the same way as micas to the velocity distribution. In contrast, quartz CPO results in slow V_P along or near the foliation plane. As a result, the overall anisotropy is nearly five times lower than the intrinsic anisotropy of biotite.

Greenschist-facies ultramylonite zone

The transition to the greenschist-facies ultramylonite (Fig.12) is characterized by striking changes of seismic properties (seismic wave velocities and anisotropy). Absolute P-wave velocities of the aggregate decrease ($6.0 < V_P < 6.6$ $km.s^{-1}$) and the strength of anisotropy increases to 10.6 % (more than twice the value calculated in the mylonite, Fig.12d). The ultramylonite has a well-defined hexagonal symmetry with a fast plane of P-wave propagation (6.5-6.6 $km.s^{-1}$) matching the foliation and a slow symmetry axis (6.0 $km.s^{-1}$) corresponding to the normal to the foliation plane (Z axis). AV_S follows the same trend with a doubling of anisotropy up to 10 % in the foliation plane, while splitting is null

when the S-wave propagates along Z. The ultramylonite is characterized by the complete breakdown of biotite and the crystallisation of more than 20 % muscovite with a very well-developed CPO parallel to the foliation (J=13.8, Fig.12a,b). As a result, muscovite shows the highest single phase seismic anisotropy, reaching 46.9 % and 50 % of AV_P and AV_S, respectively, and it controls the bulk anisotropy of the aggregate (Fig.12c). Seismic anisotropy of quartzofeldspathic phases is on average ten times lower than that of muscovite. Quartz ($AV_P = 4.2$ %) shows a slow plane at low angle from the foliation and a fast axis related to the orientation of the c-axis. Plagioclase, which represents 30 % of the rock volume, is recrystallized to oligoclase and albite. Both phases have a very weak fabric and therefore low seismic anisotropy (oligoclase ($AV_P = 3.6$ %) and albite ($AV_P = 5.3$ %, Fig.12b,c). Thus, in the ultramylonite, the main effects of quartz and oligoclase + albite is to attenuate the effect of muscovite on the bulk seismic anisotropy. The variation of the calculated seismic properties across the strain gradient is summarized in Fig.13.

4.4.2. Modelled seismic properties of a meter-scale shear zone

The aim of this section is to model the seismic properties of the meter-scale shear zone, from which the studied samples were collected, using the seismic properties calculated for each deformation stage. The natural shear zone shown in Fig.1c and d is simplified into a conceptual composite tabular shear zone (e.g. Fossen and Cavalcante, 2017, Fig.14). This conceptual model is divided into three parts: (1) the undeformed protolith, bearing a magmatic foliation normal to the shear zone margins ; (2) the amphibolite-facies shear zone, corresponding to protomylonites and mylonite, where the angle between the metamorphic foliation and the shear plane progressively decreases, from 60° in protomylonite 1 to 20° in the mylonite ; (3) the greenschist-facies ultramylonite core of the shear zone, where the metamorphic foliation is parallel to the shear plane. The high angle between foliation and shear plane in protomylonites is due to the presence of the inherited magmatic foliation, at 90° to the shear zone. The respective seismic properties (V_P, AV_P, AV_S) of the different deformation stages, shown on the left side of Fig.14, are from Fig.9d, 23d, 10d, 11d and 12d, and are rotated such that the reference frame matches the orientation of the foliation plane. The incident wave at the bottom of the model is

a cone of ray paths at 15° on either side of the vertical axis and travels normally to the shear zone. If we consider a teleseismic wave, the shear zone would be horizontal. When considering a teleseimic P-wave propagating through a full shear zone, four velocity contrasts are crossed: V_P increases by ∼8 % between the protolith and the amphibolite-facies shear zone, and decreases by ∼10 % between the mylonite and the greenschist-facies ultramylonite core.

To obtain the bulk seismic properties of the shear zone, the rotated seismic properties of each component were weighted depending on its relative volume proportion. In order to discuss the role of the three defined domains of the conceptual shear zone, three different geometries were taken into account with three disctinct high strain core versus amphibolite shear zone ratios (5, 15 and 30 % of high strain zone, respectively ; Fig.15a). The thickness of the amphibolite shear zone zone is kept constant. The geometries could also be considered as three disctinct strain and time steps of the developement of a shear zone (Fossen and Cavalcante, 2017; Means, 1995; Hull, 1988; Vitale and Mazzoli, 2008).

Results of the modelling are shown in Fig.15. For geometry I (5 % of high strain zone), V_P anisotropy can be approximated with orthorhombic symmetry, with fast and slow axes at ∼30° and 90° to the shear plane, respectively. With the progressive development of the high strain core, geometries II and III in Fig.15a show that the anisotropy progressively evolves towards a more hexagonal symmetry. The fast plane tends to become closer to the shear plane, but even when the shear zone represents approximately 50 vol.% of the considered volume (geometry III), there is still an obliquity of 15° between the fast plane and the shear plane (Fig.15b). The strength of anisotropy AV_P does not significantly increase with strain. It ranges from 4.2 % in geometry I to 4.7 % in geometry III. Although the highly anisotropic strain zone volume increases by 25 %, the increase in bulk AV_P does not exceed 12 % (Fig.15b,d). The obliquity between the anisotropic fabric and the shear plane is also reflected by AV_S. Two AV_S maxima, aligned on a plane oblique to the shear plane, are observed in geometries I and II. With the development of the ultramylonite, these maxima become more connected, defining a plane, still oblique, along which splitting is maximized, although not homogeneous (Fig.15c). AV_S is

not modified by the increasing ultramylonite versus marginal zone ratio (Fig.15d).

5. Discussion

5.1. Consistency between measured and calculated seismic properties

In the studied shear zone from the Neves area, the experimental and calculated results show good consistency, with V_P, AV_P and AV_S having similar trends for both methods. Experimentally measured V_P ranges from 5.5 to 6.5 $km.s^{-1}$ (Fig.8a), which is in good agreement with published experimental results (e.g. Jones and Nur, 1982 in the Columbia River fault zone; Barruol et al., 1992 in the San Barthelemy massif; Kästner et al., 2020 in the Seve Nappe Complex; Leclère et al., 2015 in the Argentera fault zone) and numerical studies (e.g. Barruol et al., 1992; Punturo et al., 2014 in the Kavala shear zone). Although experiments have been performed under high pressure conditions, experimental V_P is consistently lower than those calculated by microtextural EBSD analysis, by ∼3 % (Fig.8a and 13, Table 1). In contrast, AV_P is higher when estimated in laboratory than by EBSD, as previously observed by Almqvist et al. (2013) and Barruol et al. (1992) (Fig.8b, 13b, 1). This discrepancy may be due to the presence of aligned grain boundaries and microcracks that are not completely closed (Almqvist et al., 2013). It is likely that the confining pressure of 250 MPa is not sufficient to close all the microcracks, especially those with a low aspect ratio. This may cause a sligh overestimation of the measured anisotropy magnitude, but since microcracks are likely to be parallel to the prefered orientation of the grains, the presence of residual microcracks should not influence the symmetry of the anisotropic fabrics in mylonites. We also cannot rule out that the mismatch between both methods may be due to polishing issues and misindexing of phyllosilicates that tend to underestimate the contribution of phyllosilicates on modeled seismic P-wave speed anisotropy. The Y-axis concentration of mica c-axes, which contributes to reducing the overall anisotropy magnitude, can be due to the preferential indexing of the grains showing this orientation (Dempsey et al., 2011), even if the indexing strategy may have reduced this effect (see Supplementary Material S5). Furthermore, the modelling approach used to calculate bulk elastic data and infer seismic properties of the rock aggregate is based on the Voigt-Reuss-Hill average (arithmetic mean) and therefore does not take into account the effect

of the spatial arrangement of grains (microstructure) (Vel et al., 2016). Compositional layering, with aligned phyllosilicate grains is also known to affect seismic wave speed anisotropy (Naus-Thijssen et al., 2011). In our case, this effect could be neglected because there is no layering in the igneous protolith and deformation does not produce a layering with strong mineralogical contrast.

Measured and modeled AV_S (Fig.8c and 13c, Table 1) are overall very consistent, except for the X core of protomylonite 2. Our results contrast with (Almqvist et al., 2013) who observed experimental AV_S values consistently higher by 3-7 % than those calculated from a combination of EBSD and neutron diffraction data. Combining these two methods allows to test the accuracy of the reconstruction of seismic properties and to investigate the mineralogical and textural contributions of the effective properties measured in laboratory.

5.2. Evolution of bulk seismic properties with strain and metamorphism

The studied shear zone is described in three sections based on deformation and metamorphic style: (1) a protolith, (2) an amphibolite-facies strain gradient and (3) a greenschist-facies high strain zone. In this contribution, we show that the bulk seismic properties do not evolve linearly with strain.

Although the shear zone is developed in a mineralogically homogeneous plutonic rock without layering, this host rock initially exhibits a bulk seismic anisotropy that cannot be neglected from a geophysical perspective (4.6 % AV_P and 4.1 % $AV_S(max)$ calculated). It results from the presence of a weak magmatic foliation, visible in the field and mostly defined by abundant and aligned plagioclase phenocrysts. The crystallographic preferred orientation of magmatic plagioclase is such that the magmatic foliation corresponds to a slow V_P plane, oriented at high angle ($\sim$90°) to the shear zone boundaries. In the protolith, quartz and biotite grains are randomly oriented and do not contribute significantly to the bulk seismic anisotropy.

The development of the shear zone via solid state deformation under amphibolite facies is not associated with a significant change in the modal abundance of the main rock-forming phases (quartz, plagioclase and biotite) except for the crystallization of $\sim$5 % muscovite. Indeed, at the inferred P-T conditions of the onset of deformation (ca. 500°C and 0.6 GPa) there is no major phase transition

(Fig.6) that could explain the evolution of seismic properties between the protolith and the deformed zone. The major change is the development of a composite structure that consists of foliation and shear planes (S-C structure) combined with the recrystallization of plagioclase, quartz and biotite. With increasing strain, the fabric becomes very well defined with the development of interconnected plagioclase weak layers, alignment of phyllosilicates and the progressive rotation of the foliation plane (S) towards the shear plane (C) orientation. This structural change induces an increase of P-wave fastest velocities and anisotropy, which reaches maximum values of 12 % for AV_P and 7 % for AV_S in the protomylonite. However, in the higher strain mylonite, the strong decrease of AV_P and AV_S, which drop down to ∼5 % and ∼3-5 % respectively, cannot be diretly accounted for by either the fabric transition or the mineralogical evolution.

We suggest that this non-linear evolution of seismic properties with strain, and more particularly the decrease of anisotropy in the mylonite, is related to the evolution of crystallographic preferred orientations of the rock-forming minerals. Specifically, it is due to the interference between strongly anisotropic minerals (e.g phyllosilicates) and less anisotropic but more abundant phases (e.g. quartz and plagioclase). The interaction between quartz and muscovite has already been explored by Naus-Thijssen et al. (2011) and Ward et al. (2012), which demonstrated, using either synthetic or natural rock samples, that muscovite-induced anisotropy can be overwhelmed by the orientation of less anisotropic matrix grains and more particularly in mica-poor rocks. In the amphibolite-facies section of the studied shear zone, the destructive effect of quartz is shown by the geometry of P-wave velocities V_P and S-wave anisotropy AV_S (Fig.23,10,11). With 19 to 13 volume % of phyllosilicates, we could expect a hexagonal symmetry of both V_P and AV_S but the active slip system for quartz (basal <a>) results in the alignment of the fast c-axis perpendicular to the fast cleavage plane of phyllosilicates. This results in an orthorhombic symmetry for all the samples belonging to the amphibolite-facies shear zone section, with a fast axis corresponding to the lineation (X) and a slow axis perpendicular to the foliation (Z) and an intermediate axis (Y) that corresponds to the intersection fo S- and C-planes. Although plagioclase represents almost ∼50 % of the rock volume of the amphibolite-facies shear zone, its CPO is so weak

that it could be considered as quasi-isotropic with respect to seismic wave speed behaviour. Even if the (100)<001> slip system alignes its fast axis with the lineation, the main effect of plagioclase is to mute to some extent the high values of seismic anisotropy associated with phyllosilicates. The unexpected decrease of seismic anisotropy magnitude in the mylonite is incompletely understood. It is not related to a strengthening of the quartz contribution: in contrast with protomylonites, where deformation is more likely controled by dislocation creep, it has been shown that diffusion creep can become more important in the higher strained parts of shear zones, producing weaker CPO (e.g. Condit and Mahan, 2018; Oliot et al., 2014; Wehrens et al., 2016). In particular, it can explain the absence of significant CPO in plagioclase, where granular flow is likely to be dominant (e.g. Oliot et al., 2014). This variation in the dominant deformation mechanism could thus play a role in the loss of seismic anisotropy in mylonites. But despite the potential effect of deformation mechanisms, this decrease seems more probably related to a weakening of the phyllosilicate contribution. First, the amount of phyllosilicates in the mylonite decreases to 13 % (instead of 19-18 % in the protomylonite). Second, and perhaps most importantly, we observe a weakening of their fabric strength and therefore of their contribution to the bulk seismic anisotropy (Fig.11). Indeed, the breakdown of biotite due to the evolution of the metamorphic conditions initiates in the mylonite, and is not counterbalanced yet by the crystallization of muscovite, only observed in the ultramylonite. Our observations are consistent with numerical and experimental studies showing that seismic anisotropy can decrease in the most deformed stages, unless a sufficient modal fraction of well-oriented micas could balance this effect (e.g. Jones and Nur, 1982; Barruol et al., 1992; Tatham et al., 2008; Wenning et al., 2016).

The evolution of seismic properties in the high strain core of the shear zone, corresponding to an increase of AV_P and AV_S up to 10 and 7 %, respectively, in the ultramylonite, is consistent with experimental and numerical values (6-18 %) obtained on mylonitized granites (Jones and Nur, 1982, 1984; Barruol et al., 1992; Lloyd et al., 2009). This evolution observed along the gradient is directly related to change in syn-kinematic metamorphic conditions and therefore mineralogy. In granitic rocks, the transition from amphibolite- to greenschist-facies conditions during cooling from 500 to

450°C corresponds to the univariant reaction in the NaCaKFMASH system : plagioclase + biotite + K-feldspar + quartz + H2O = muscovite + chlorite + albite + epidote (Fig.6). This transition results in the crystallization of more than 20 % muscovite and chlorite and the recrystallization of plagioclase into a fine grain aggregate of albite and oligoclase. It is also accompanied by a switch in the dominant active slip system in quartz (from basal <a> to rhomb <a>). Among all these changes, the crystallization of very well aligned muscovite in the shear plane has the most profound effect on seismic properties (Fig.12). The geometry of the P-wave velocity distribution and the anisotropy of S-wave exhibits a strong hexagonal symmetry with a fast V_P plane, and strong S-wave splitting with fast polarization along the shear plane. Quartz and plagioclase do not modify the geometry of the seismic properties but attenuate the intensity of anisotropy of the bulk aggregate.

5.3. Imaging of crustal shear zones based on seismic anisotropy

Only shear zones with a thickness higher than ∼2 km can be properly imaged by teleseismic technics like receiver functions (Schulte-Pelkum and Mahan, 2014). Many structural studies carried on exhumed km-scale shear zones have described them as very complex and heterogeneous deformation regions. They consists of a network of anastomosed high-strain zones surrounding low-strain lenses, as described for example in Cap de Creus (Spain; Carreras, 2001, e.g.) or in the East Tenda shear zone (Corsica, France; Molli et al., 2006, e.g.). This anastomosed geometry can be observed at all scales, from resistant feldspar lenses embedded in micas-rich matrix at the microscale, to plutonic domains of several hundreds of kilometers surrounded by kilometer-wide mylonite zones (e.g. Fossen and Cavalcante, 2017). Modelling the teleseismic signature of anastomosed crustal-scale shear zone is therefore a complex task that depends widely on the geometry. In this contribution, we focus on the seismic signature of a simplified single strain gradient, from the weakly deformed domains to the high-strain zone.

Our reconstruction of the seismic properties of the whole strain gradient highlights the major role of the amphibolite-facies marginal zone, which induces an orthorhombic symmetry in the spatial distribution of V_P and an obliquity between the shear plane and the fast P-wave propagation plane

(Fig.15). While some prior studies have also emphasized the potential importance of shear zone strain gradients (e.g. Rey et al., 1994), others have assumed that the seismic properties of shear zones are controlled by the ultramylonite core (e.g. Jones and Nur, 1984; Christensen and Szymanski, 1988; McDonough and Fountain, 1988, 1993), which shows a strong velocity contrast with the surrounding rock. In a natural shear zone, the progressive rotation of the foliation plane in the protomylonitic margin causes a more gradual decrease of V_P in a direction normal to the shear plane, marked by two velocity contrasts, between the protolith and the shear zone margins, and between the shear zone margins and the ultramylonite core.

Imaging crustal shear zones requires to compute synthetic seismograms associated with a geological model that shows the spatial variations of physical properties of the rocks (e.g. Schulte-Pelkum and Mahan, 2014). Most models used in geophysical studies assumed an homogeneous anisotropic fabric within shear zones, reflecting either the oblique fabric of the marginal orthorhombic zone (Fig.16a, e.g. Zandt et al., 2004; Schulte-Pelkum et al., 2005) or the parallelized fabric of the ultramylonite (Fig.16b, e.g. Schulte-Pelkum and Mahan, 2014). The aim of the present contribution is to include also the role of strain gradient of the shear zones. The integrated AV_P estimated in this study for the whole shear zone including the amphibolite-facies margins with an orthorhombic symmetry does not exceed 5 %, despite an AV_P higher than 10 % in the ultramylonite. Thus, the role of the S plane-dominated marginal zone may need to be taken into account in the elaboration of the synthetic seismograms. Furthermore, the role of the protolith cannot be neglected, since it can bear an inherited anisotropic fabric which may impact the strength and the orientation of the seismic properties of the whole shear zone. We thus propose a new model based on the spatial variability of the seismic properties observed accross the strain gradient. Our model includes (1) an anisotropic protolith, and a deformed zone composed of (2) an amphibolite-facies marginal zone characterized by an orthorhombic symmetry which fast axis is at 30° from the shear zone boundaries and (3) a greenschist-facies ultramylonitic core with a hexagonal symmetry which fast plane is parallel to the shear plane (Fig.16c). This model does not take into account all the complexity of the transition zone, i.e. the progressive rotation of the foliation and the

decrease of anisotropy in mylonite. However, it highlights a more realistic view of shear zones and could contribute to solving uncertainities in the interpretation of geophysical imaging. For instance, Schulte-Pelkum et al. (2005) have observed an obliquity between the expected and measured fast planes within the Main Himalayan Thrust. Actually, the detected anisotropic fabric is oriented 40° from the thrust plane. According to our model, and assuming that it can be upscaled as explained above, this detected anisotropy could be explained by the presence of the transition zone which presents similar anisotropy magnitude as the ultramylonitic core, and most likely controls the global orientation of the anisotropic fabric. However, we have shown that the metamorphic conditions of deformation, i.e. the reequilibration into greenschist-facies conditions, strongly influence the seismic properties of the studied shear zone by modifying texture and mineralogy in the ultramylonite zone. Thus, the seismic properties of crustal-scale strain zones spanning a wide range of pressure and temperature conditions must integrate the effect of the various metamorphic conditions through the full extent of the discontinuity.

6. Conclusions

Ultrasonic laboratory measurements and calculations from petrofabrics exhibit a complex transition in the seismic properties across the studied shear zone strain gradient. The expected continuous increase of the magnitude of seismic anisotropy with strain is disrupted by a large reduction of the anisotropy in the mylonite, despite the progressive development of the foliation parallel to the shear plane. The seismic properties are mainly controlled by the behavior of phyllosilicates and by the destructive interference from the more weakly anisotropic quartzo-feldspathic phases. The results also highlight the importance of the metamorphic conditions. Deformation in protomylonites and mylonite developed under amphibolite-facies conditions without signficant major mineral transformation. Here, a S-C composite structure is defined by metamorphic biotite and influenced by locally preserved magmatic biotite. In contrast, the retrogression under greenschist-facies conditions in the ultramylonite induces a C-dominated structure, characterized by the complete replacement of biotite by muscovite and chlorite. In summary, under amphibolite- to greenschist-facies conditions, the seismic properties

of shear zones may be largely controlled by the orthorhombic symmetry preserved in the transitional margin of the strain gradients, consistent with oblique anisotropic fabrics associated with shear zones imaged in some geophysical studies. While the high-strain ultramylonites have often be regarded as the main source of seismic anisotropy within shear zones, this study highlights the important contribution of the protolith and the shear zone margins, which should be taken into account to predict the geophysical signature of crustal-scale shear zones.

7. Acknowledgements

This work was supported by Ministère de l'Enseignement Supérieur et de la Recherche, the CNRS INSU TelluS–SYSTER 2018 and 2019, Observatoire des Sciences de l'Univers Theta Bourgogne – Franche-Comté, Ecole Doctorale Environnement-Santé, and National Science Foundation grant EAR 1252295. Philippe Goncalves acknowledges Région Bourgogne Franche-Comté, programme mobilité sortante 2018Y-05660. The authors warmly thank the PEA2t platform (Chrono-environnement, University Bourgogne Franche-Comté, UMR CNRS 6249, France), which manages and maintains the analytical equipment used in this study. We greatly acknowledge the Department of Geological Sciences and the Colorado Shared Instrumentation in Nanofabrication and Characterization of the University of Colorado Boulder (USA), and the Rock Deformation Laboratory of the University of Liverpool (UK), for hosting us for the acquisition and processing of the EBSD and experimental data, respectively. Special thanks to Didier Convert-Gaubier for the thin-section preparation and John Bedford, Gary Coughlan, and Michael Allen for their precious help during the laboratory measurements.

References

Aleksandrov, K., TV, R., 1961. The elastic properties of rock forming minerals ii: Layered silicates. Bull. Acad. Sci. USSR, Geophys. Ser. 9, 1165–1168.

Almqvist, B.S.G., Hirt, A.M., Herwegh, M., Ebert, A., Walter, J.M., Leiss, B., Burlini, L., 2013. Seismic anisotropy in the Morcles nappe shear zone: Implications for seismic imaging of crustal

scale shear zones. Tectonophysics 603, 162–178. URL: http://www.sciencedirect.com/science/article/pii/S0040195113003375, doi:10.1016/j.tecto.2013.05.025.

Armitage, P.J., Faulkner, D.R., Worden, R.H., Aplin, A.C., Butcher, A.R., Iliffe, J., 2011. Experimental measurement of, and controls on, permeability and permeability anisotropy of caprocks from the co2 storage project at the krechba field, algeria. Journal of Geophysical Research: Solid Earth 116. URL: https://agupubs.onlinelibrary.wiley.com/doi/abs/10.1029/2011JB008385, doi:https://doi.org/10.1029/2011JB008385, arXiv:https://agupubs.onlinelibrary.wiley.com/doi/pdf/10.1029/2011JB008385.

Barruol, G., Mainprice, D., Kern, H., de Saint Blanquat, M., Compte, P., 1992. 3d seismic study of a ductile shear zone from laboratory and petrofabric data (Saint Barthélémy Massif, Northern Pyrenees, France). Terra Nova 4, 63–76. doi:10.1111/j.1365-3121.1992.tb00451.x.hal-01389722.

Birch, F., 1960. The velocity of compressional waves in rocks to 10 kilobars: 1. Journal of Geophysical Research 65, 1083–1102. URL: http://onlinelibrary.wiley.com/doi/10.1029/JZ065i004p01083/abstract, doi:10.1029/JZ065i004p01083.

Blake, O.O., 2011. Seismic transport properties of fractured rocks. Ph.D.. University of Liverpool. URL: https://ethos.bl.uk/OrderDetails.do?uin=uk.bl.ethos.569902.

Blake, O.O., Faulkner, D.R., Rietbrock, A., 2013. The Effect of Varying Damage History in Crystalline Rocks on the P- and S-Wave Velocity under Hydrostatic Confining Pressure. Pure and Applied Geophysics 170, 493–505. URL: http://link.springer.com/article/10.1007/s00024-012-0550-0, doi:10.1007/s00024-012-0550-0.

Brown, J.M., Angel, R.J., Ross, N.L., 2016. Elasticity of plagioclase feldspars. Journal of Geophysical Research: Solid Earth 121, 663–675.

Bunge, H.J., Esling, C., 1982. Quantitative texture analysis. Deutsche Gesellschaft fur Metallkunde, v+ 551, 24 x 17 cm, illustrated(DM 168. 00 .

Bunge, H.J., Kiewel, R., Reinert, T., Fritsche, L., 2000. Elastic properties of polycrystals—influence of texture and stereology. Journal of the Mechanics and Physics of Solids 48, 29–66. URL: http://www.sciencedirect.com/science/article/pii/S0022509699000204, doi:10.1016/S0022-5096(99)00020-4.

Burdick, L.J., Langston, C.A., 1977. Modeling crustal structure through the use of converted phases in teleseismic body-wave forms. Bulletin of the Seismological Society of America 67, 677–691. URL: https://pubs.geoscienceworld.org/bssa/article-abstract/67/3/677/117706/Modeling-crustal-structure-through-the-use-of.

Carreras, J., 2001. Zooming on northern cap de creus shear zones. Journal of Structural Geology 23, 1457–1486.

Choukroune, P., Gapais, D., 1983. Strain pattern in the Aar Granite (Central Alps): orthogneiss developed by bulk inhomogeneous flattening. Journal of Stuctural Geology 5 (3-4), 411–418.

Christensen, J.N., Selverstone, J., Rosenfeld, J.L., DePaolo, D.J., 1994. Correlation by Rb-Sr geochronology of garnet growth histories from different structural levels within the Tauern Window, Eastern Alps. Contributions to Mineralogy and Petrology 118, 1–12.

Christensen, N.I., 1965. Compressional wave velocities in metamorphic rocks at pressures to 10 kilobars. Journal of Geophysical Research 70, 6147–6164.

Christensen, N.I., Szymanski, D.L., 1988. Origin of reflections from the Brevard Fault Zone. Journal of Geophysical Research: Solid Earth 93, 1087–1102. URL: https://agupubs.onlinelibrary.wiley.com/doi/abs/10.1029/JB093iB02p01087, doi:https://doi.org/10.1029/JB093iB02p01087.

Chroston, P.N., Max, M.D., 1988. Seismic anisotropy in mylonites: an example from the Mannin Thrust Zone, southwest Connemara, Ireland. Tectonophysics 148, 29–39. URL: http://www.sciencedirect.com/science/article/pii/0040195188901588, doi:10.1016/0040-1951(88)90158-8.

Condit, C.B., Mahan, K.H., 2018. Fracturing, fluid flow and shear zone development: Relationships between chemical and mechanical processes in proterozoic mafic dykes from southwestern montana, usa. Journal of Metamorphic Geology 36, 195–223.

Connolly, J.A.D., 2005. Computation of phase equilibria by linear programming: A tool for geodynamic modeling and its application to subduction zone decarbonation. Earth and Planetary Science Letters 236, 524–541. URL: http://www.sciencedirect.com/science/article/pii/S0012821X05002839, doi:10.1016/j.epsl.2005.04.033.

Connolly, J.A.D., Kerrick, D.M., 1987. An algorithm and computer program for calculating composition phase diagrams. Calphad 11, 1–55. URL: http://www.sciencedirect.com/science/article/pii/0364591687900186, doi:10.1016/0364-5916(87)90018-6.

Dempsey, E., Prior, D., Mariani, E., Toy, V., Tatham, D., 2011. Mica-controlled anisotropy within mid-to-upper crustal mylonites: an EBSD study of mica fabrics in the Alpine Fault Zone, New Zealand. Geological Society of London Special Publications 360, 33–47. doi:10.1144/SP360.3.

Diehl, T., Husen, S., Kissling, E., Deichmann, N., 2009. High-resolution 3-d p-wave model of the alpine crust. Geophysical Journal International 179, 1133–1147. URL: https://onlinelibrary.wiley.com/doi/abs/10.1111/j.1365-246X.2009.04331.x, doi:https://doi.org/10.1111/j.1365-246X.2009.04331.x, arXiv:https://onlinelibrary.wiley.com/doi/pdf/10.1111/j.1365-246X.2009.04331.x.

Fossen, H., Cavalcante, G.C.G., 2017. Shear zones – A review. Earth-Science Reviews 171, 434–455. URL: http://www.sciencedirect.com/science/article/pii/S0012825217300272, doi:10.1016/j.earscirev.2017.05.002.

Fountain, D.M., 1976. The ivrea—verbano and strona-ceneri zones, northern italy: a cross-section of the continental crust—new evidence from seismic velocities of rock samples. Tectonophysics 33, 145–165.

Fusseis, F., Handy, M., 2008. Micromechanisms of shear zone propagation at the brittle–viscous transition. Journal of Structural Geology 30, 1242–1253.

Fusseis, F., Handy, M., Schrank, C., 2006. Networking of shear zones at the brittle-to-viscous transition (Cap de Creus, NE Spain). Journal of Structural Geology 28, 1228–1243. URL: http://linkinghub.elsevier.com/retrieve/pii/S0191814106000757, doi:10.1016/j.jsg.2006.03.022.

Glodny, J., Ring, U., Kühn, A., 2008. Coeval high-pressure metamorphism, thrusting, strike-slip, and extensional shearing in the Tauern Window, Eastern Alps: TAUERN WINDOW EVOLUTION. Tectonics 27, n/a–n/a. URL: http://doi.wiley.com/10.1029/2007TC002193, doi:10.1029/2007TC002193.

Goncalves, P., Oliot, E., Marquer, D., Connolly, J., 2012. Role of chemical processes on shear zone formation: an example from the grimsel metagranodiorite (aar massif, central alps). Journal of Metamorphic Geology 30, 703–722.

Guillope, M., Poirier, J.P., 1979. Dynamic recrystallization during creep of single-crystalline halite: An experimental study. Journal of Geophysical Research: Solid Earth 84, 5557–5567. URL: https://agupubs.onlinelibrary.wiley.com/doi/abs/10.1029/JB084iB10p05557, doi:10.1029/JB084iB10p05557.

Hayman, N.W., Lavier, L.L., 2014. The geologic record of deep episodic tremor and slip. Geology 42, 195–198.

Hielscher, R., Schaeben, H., 2008. A novel pole figure inversion method: specification of the mtex algorithm. Journal of Applied Crystallography 41, 1024–1037.

Hill, R., 1952. The Elastic Behaviour of a Crystalline Aggregate. Proceedings of the Physical Society. Section A 65, 349–354. URL: https://doi.org/10.1088%2F0370-1298%2F65%2F5%2F307, doi:10.1088/0370-1298/65/5/307.

Hull, J., 1988. Thickness-displacement relationships for deformation zones. Journal of Structural Geology 10, 431–435.

Ji, S., Salisbury, M.H., 1993. Shear-wave velocities, anisotropy and splitting in high-grade mylonites. Tectonophysics 221, 453–473. URL: https://www.sciencedirect.com/science/article/pii/004019519390173H, doi:https://doi.org/10.1016/0040-1951(93)90173-H.

Jiang, F., Speziale, S., Shieh, S.R., Duffy, T.S., 2004. Single-crystal elasticity of andradite garnet to 11 gpa. Journal of Physics: Condensed Matter 16, S1041.

Jones, T., Nur, A., 1982. Seismic velocity and anisotropy in mylonites and the reflectivity of deep crystal fault zones. Geology 10, 260–263. URL: https://pubs.geoscienceworld.org/geology/article-abstract/10/5/260/189662/Seismic-velocity-and-anisotropy-in-mylonites-and, doi:10.1130/0091-7613(1982)10<260:SVAAIM>2.0.CO;2.

Jones, T.D., Nur, A., 1984. The nature of seismic reflections from deep crustal fault zones. Journal of Geophysical Research: Solid Earth 89, 3153–3171. URL: https://agupubs.onlinelibrary.wiley.com/doi/abs/10.1029/JB089iB05p03153, doi:10.1029/JB089iB05p03153.

Kästner, F., Pierdominici, S., Elger, J., Zappone, A., Kück, J., Berndt, C., 2020. Correlation of core and downhole seismic velocities in high-pressure metamorphic rocks: a case study for the cosc-1 borehole, sweden. Solid Earth 11, 607–626.

Kern, H., Wenk, H.R., 1990. Fabric-related velocity anisotropy and shear wave splitting in rocks from the santa rosa mylonite zone, california. Journal of Geophysical Research: Solid Earth 95, 11213–11223. URL: https://agupubs.onlinelibrary.wiley.com/doi/abs/10.1029/JB095iB07p11213, doi:https://doi.org/10.1029/JB095iB07p11213, arXiv:https://agupubs.onlinelibrary.wiley.com/doi/pdf/10.1029/JB095iB07p11213.

Leclère, H., Cappa, F., Faulkner, D., Fabbri, O., Armitage, P., Blake, O., 2015. Development and maintenance of fluid overpressures in crustal fault zones by elastic compaction and implications for

748 earthquake swarms. Journal of Geophysical Research: Solid Earth , 2014JB011759URL: http://
749 onlinelibrary.wiley.com/doi/10.1002/2014JB011759/abstract, doi:10.1002/2014JB011759.

750 Lloyd, G.E., Butler, R.W.H., Casey, M., Mainprice, D., 2009. Mica, deformation fabrics and
751 the seismic properties of the continental crust. Earth and Planetary Science Letters 288, 320–
752 328. URL: http://www.sciencedirect.com/science/article/pii/S0012821X0900569X, doi:10.
753 1016/j.epsl.2009.09.035.

754 Mainprice, D., 1990. A FORTRAN program to calculate seismic anisotropy from the lattice preferred
755 orientation of minerals. Computers & Geosciences 16, 385–393. URL: http://www.sciencedirect.
756 com/science/article/pii/0098300490900722, doi:10.1016/0098-3004(90)90072-2.

757 Mainprice, D., 2007. The Seismological Signature of Plastic Flow in Subduction Zones: a Rock Physics
758 Perspective. Subduction Dynamics: Bridging the Scales , 34.

759 Mainprice, D., Bouchez, J.L., Blumenfeld, P., Tubià, J.M., 1986. Dominant c slip in
760 naturally deformed quartz: Implications for dramatic plastic softening at high tem-
761 perature. Geology 14, 819–822. URL: https://pubs.geoscienceworld.org/geology/
762 article-abstract/14/10/819/203864/Dominant-c-slip-in-naturally-deformed-quartz,
763 doi:10.1130/0091-7613(1986)14<819:DCSIND>2.0.CO;2.

764 Mainprice, D., Casey, M., 1990. The calculated seismic properties of quartz mylonites with typical
765 fabrics: relationship to kinematics and temperature. Geophysical Journal International 103, 599–608.
766 URL: https://academic.oup.com/gji/article/103/3/599/586939, doi:10.1111/j.1365-246X.
767 1990.tb05674.x.

768 Mainprice, D., Hielscher, R., Schaeben, H., 2011. Calculating anisotropic physical properties from
769 texture data using the MTEX open-source package. Geological Society, London, Special Publications
770 360, 175–192. URL: https://sp.lyellcollection.org/content/360/1/175, doi:10.1144/SP360.
771 10.

Mainprice, D., Humbert, M., 1994. Methods of calculating petrophysical properties from lattice preferred orientation data. Surveys in Geophysics 15, 575–592. URL: https://doi.org/10.1007/BF00690175, doi:10.1007/BF00690175.

Mancktelow, N.S., Pennacchioni, G., 2005. The control of precursor brittle fracture and fluid–rock interaction on the development of single and paired ductile shear zones. Journal of Structural Geology 27, 645–661. URL: http://linkinghub.elsevier.com/retrieve/pii/S0191814104002056, doi:10.1016/j.jsg.2004.12.001.

McDonough, D.T., Fountain, D.M., 1988. Reflection characteristics of a mylonite zone based on compressional wave velocities of rock samples. Geophysical Journal International 93, 547–558. URL: https://academic.oup.com/gji/article/93/3/547/662387, doi:10.1111/j.1365-246X.1988.tb03880.x.

McDonough, D.T., Fountain, D.M., 1993. P-wave anisotropy of mylonitic and infrastructural rocks from a Cordilleran core complex: the Ruby-East Humboldt Range, Nevada. Physics of the Earth and Planetary Interiors 78, 319–336. URL: http://www.sciencedirect.com/science/article/pii/0031920193901634, doi:10.1016/0031-9201(93)90163-4.

Means, W., 1995. Shear zones and rock history. Tectonophysics 247, 157–160.

Molli, G., Tribuzio, R., Marquer, D., 2006. Deformation and metamorphism at the eastern border of the tenda massif (ne corsica): a record of subduction and exhumation of continental crust. Journal of Structural Geology 28, 1748–1766.

Morteani, G., 1974. Petrology of the Tauern Window, Austrian Alps. Fortschritte der Mineralogie 52, 195–220.

Naus-Thijssen, F.M., Goupee, A.J., Vel, S.S., Johnson, S.E., 2011. The influence of microstructure on seismic wave speed anisotropy in the crust: Computational analysis of quartz-muscovite rocks. Geophysical Journal International 185, 609–621.

796 Ogi, H., Ohmori, T., Nakamura, N., Hirao, M., 2006. Elastic, anelastic, and piezoelectric coefficients of
797 α-quartz determined by resonance ultrasound spectroscopy. Journal of applied physics 100, 053511.

798 Oliot, E., Goncalves, P., Marquer, D., 2010. Role of plagioclase and reaction softening in a metagranite
799 shear zone at mid-crustal conditions (gotthard massif, swiss central alps). Journal of Metamorphic
800 Geology 28, 849–871.

801 Oliot, E., Goncalves, P., Schulmann, K., Marquer, D., Lexa, O., 2014. Mid-crustal shear zone formation
802 in granitic rocks: Constraints from quantitative textural and crystallographic preferred orientations
803 analyses. Tectonophysics 612, 63–80.

804 Pennacchioni, G., Mancktelow, N.S., 2007. Nucleation and initial growth of a shear zone network
805 within compositionally and structurally heterogeneous granitoids under amphibolite facies condi-
806 tions. Journal of Structural Geology 29, 1757–1780. URL: http://linkinghub.elsevier.com/
807 retrieve/pii/S0191814107001101, doi:10.1016/j.jsg.2007.06.002.

808 Phinney, R.A., 1964. Structure of the Earth's crust from spectral behavior of long-period body
809 waves, in: Journal of Geophysical Research (1896-1977). volume 69, pp. 2997–3017. URL:
810 https://agupubs.onlinelibrary.wiley.com/doi/abs/10.1029/JZ069i014p02997.

811 Prior, D.J., Mariani, E., Wheeler, J., 2009. Ebsd in the earth sciences: applications, common practice,
812 and challenges, in: Electron backscatter diffraction in materials science. Springer, pp. 345–360.

813 Punturo, R., Cirrincione, R., Fazio, E., Fiannacca, P., Kern, H., Mengel, K., Ortolano, G., Pezzino, A.,
814 2014. Microstructural, compositional and petrophysical properties of mylonitic granodiorites from
815 an extensional shear zone (Rhodope Core complex, Greece). Geological Magazine 151, 1051–1071.
816 URL: https://pubs.geoscienceworld.org/geolmag/article-abstract/151/6/1051/300769/
817 Microstructural-compositional-and-petrophysical, doi:10.1017/S001675681300109X.

818 Reuss, A., 1929. Calculation of the flow limits of mixed crystals on the basis of the plasticity of
819 monocrystals. Z. Angew. Math. Mech 9, 49–58.

Rey, P.F., Fountain, D.M., Clement, W.P., 1994. P wave velocity across a noncoaxial ductile shear zone and its associated strain gradient: Consequences for upper crustal reflectivity. Journal of Geophysical Research: Solid Earth 99, 4533–4548.

Ryzhova, T., Aleksandrov, K., Korobkova, V., 1966. The elastic properties of rock-forming minerals; v, additional data on silicates. Physics of the Solid Earth 2, 63–65.

Schmid, S.M., Scharf, A., Handy, M.R., Rosenberg, C.L., 2013. The Tauern Window (Eastern Alps, Austria): a new tectonic map, with cross-sections and a tectonometamorphic synthesis. Swiss Journal of Geosciences 106, 1–32. URL: http://link.springer.com/10.1007/s00015-013-0123-y, doi:10.1007/s00015-013-0123-y.

Schulte-Pelkum, V., Mahan, K.H., 2014. Imaging Faults and Shear Zones Using Receiver Functions. Pure and Applied Geophysics 171, 2967–2991. URL: http://link.springer.com/10.1007/s00024-014-0853-4, doi:10.1007/s00024-014-0853-4.

Schulte-Pelkum, V., Monsalve, G., Sheehan, A., Pandey, M.R., Sapkota, S., Bilham, R., Wu, F., 2005. Imaging the Indian subcontinent beneath the Himalaya. Nature 435, 1222–1225.

Segall, P., Simpson, C., 1986. Nucleation of ductile shear zones on dilatant fractures. Geology 14, 56–59.

Sibson, R., 1977. Fault rocks and fault mechanisms. Journal of the Geological Society 133, 191–213.

Stipp, M., Stünitz, H., Heilbronner, R., Schmid, S.M., 2002. Dynamic recrystallization of quartz: correlation between natural and experimental conditions. Geological Society, London, Special Publications 200, 171–190. URL: https://sp.lyellcollection.org/content/200/1/171, doi:10.1144/GSL.SP.2001.200.01.11.

Tatham, D., Lloyd, G., Butler, R., Casey, M., 2008. Amphibole and lower crustal seismic properties. Earth and Planetary Science Letters 267, 118–128. URL: http://linkinghub.elsevier.com/retrieve/pii/S0012821X07007650, doi:10.1016/j.epsl.2007.11.042.

Urai, J.L., Means, W.D., Lister, G.S., 1986. Dynamic Recrystallization of Minerals, in: Mineral and Rock Deformation. American Geophysical Union (AGU), pp. 161–199. URL: https://agupubs.onlinelibrary.wiley.com/doi/abs/10.1029/GM036p0161, doi:10.1029/GM036p0161.

Vaughan, M.T., Guggenheim, S., 1986. Elasticity of muscovite and its relationship to crystal structure. Journal of Geophysical Research: Solid Earth 91, 4657–4664.

Vel, S.S., Cook, A.C., Johnson, S.E., Gerbi, C., 2016. Computational homogenization and micromechanical analysis of textured polycrystalline materials. Computer Methods in Applied Mechanics and Engineering 310, 749–779.

Vitale, S., Mazzoli, S., 2008. Heterogeneous shear zone evolution: the role of shear strain hardening/softening. Journal of Structural Geology 30, 1383–1395.

Voigt, W., 1928. Lehrbuch der kristallphysik. volume 962. Teubner Leipzig.

Waeselmann, N., Brown, J.M., Angel, R.J., Ross, N., Zhao, J., Kaminsky, W., 2016. The elastic tensor of monoclinic alkali feldspars. American Mineralogist 101, 1228–1231.

Ward, D., Mahan, K., Schulte-Pelkum, V., 2012. Roles of quartz and mica in seismic anisotropy of mylonites. Geophysical Journal International 190, 1123–1134. URL: https://academic.oup.com/gji/article/190/2/1123/644149, doi:10.1111/j.1365-246X.2012.05528.x.

Wehrens, P., Berger, A., Peters, M., Spillmann, T., Herwegh, M., 2016. Deformation at the frictional-viscous transition: Evidence for cycles of fluid-assisted embrittlement and ductile deformation in the granitoid crust. Tectonophysics 693, 66–84.

Wenning, Q.C., Almqvist, B.S., Hedin, P., Zappone, A., 2016. Seismic anisotropy in mid to lower orogenic crust: Insights from laboratory measurements of vp and vs in drill core from central scandinavian caledonides. Tectonophysics 692, 14–28.

Whitney, D.L., Evans, B.W., 2010. Abbreviations for names of rock-forming minerals. American mineralogist 95, 185–187.

868 Zandt, G., Gilbert, H., Owens, T.J., Ducea, M., Saleeby, J., Jones, C.H., 2004. Active foundering of
869 a continental arc root beneath the southern Sierra Nevada in California. Nature 431, 41–46. URL:
870 https://www.nature.com/articles/nature02847, doi:10.1038/nature02847.

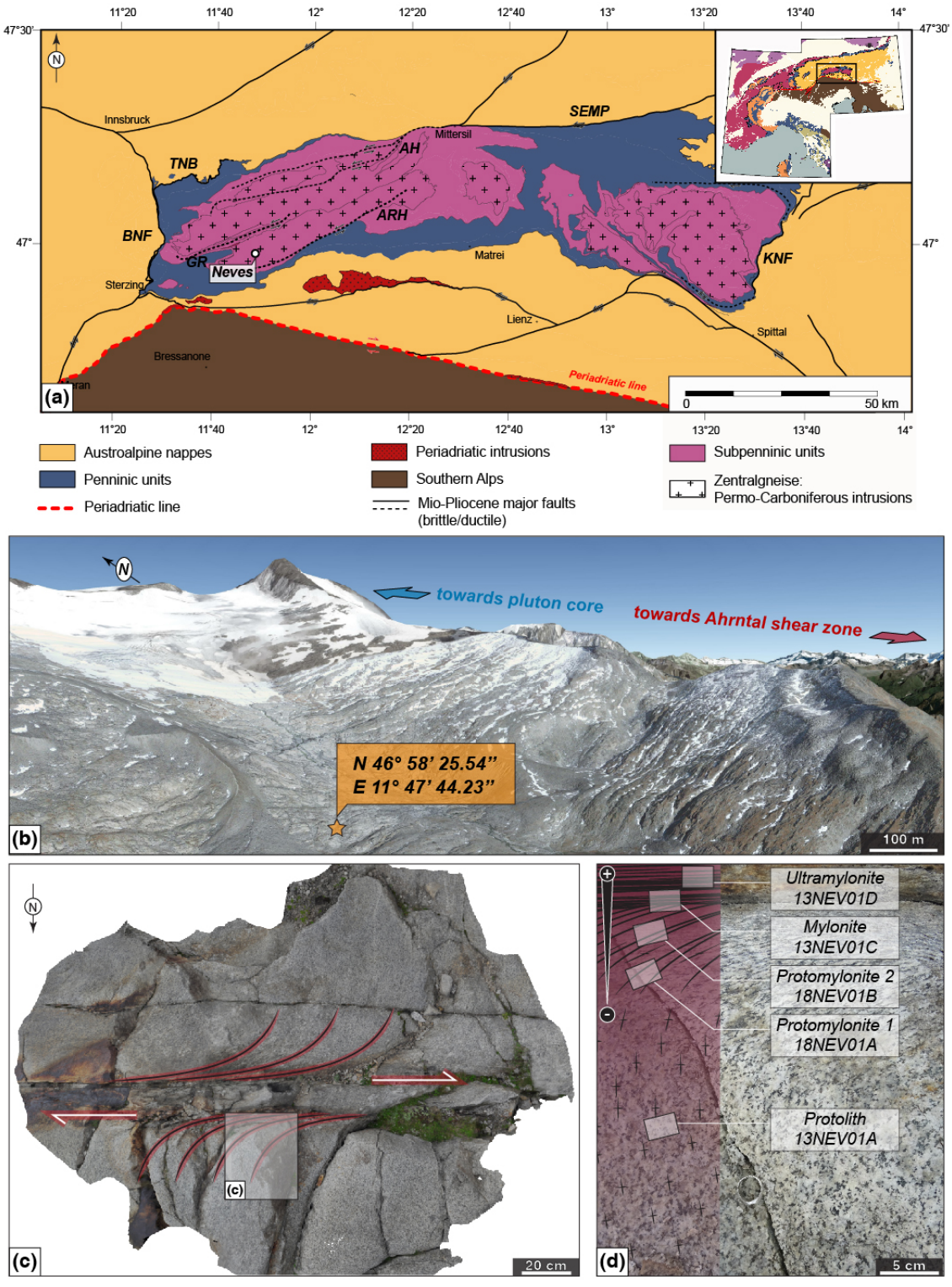

Figure 1: *(2-column fitting image)* Sampling area (a) Simplified tectonic map of the Tauern Window (modified from Schmid et al., 2013). The sampling area of Neves is highlighted by the white circle. AH Ahorn shear zone, AHR Ahrntal shear zone, BNF Brenner Normal Fault, KNF Katschberg Normal Fault, SEMP Salzach-Ennstal-Mariazell-Puchberg fault, TNB Tauern Northern Boundary fault. (b) View of the Neves area. The orange star and the coordinates indicate the location of the studied outcrop. (c) Photogrammetry picture of the studied outcrop,a m-wide dextral shear zone (top view). The white arrows indicate the kinematics, and the black lines materialize the metamorphic foliation. The square indicates the location of (d). (d) Samples location on the ductile strain gradient. The black arrow on the left

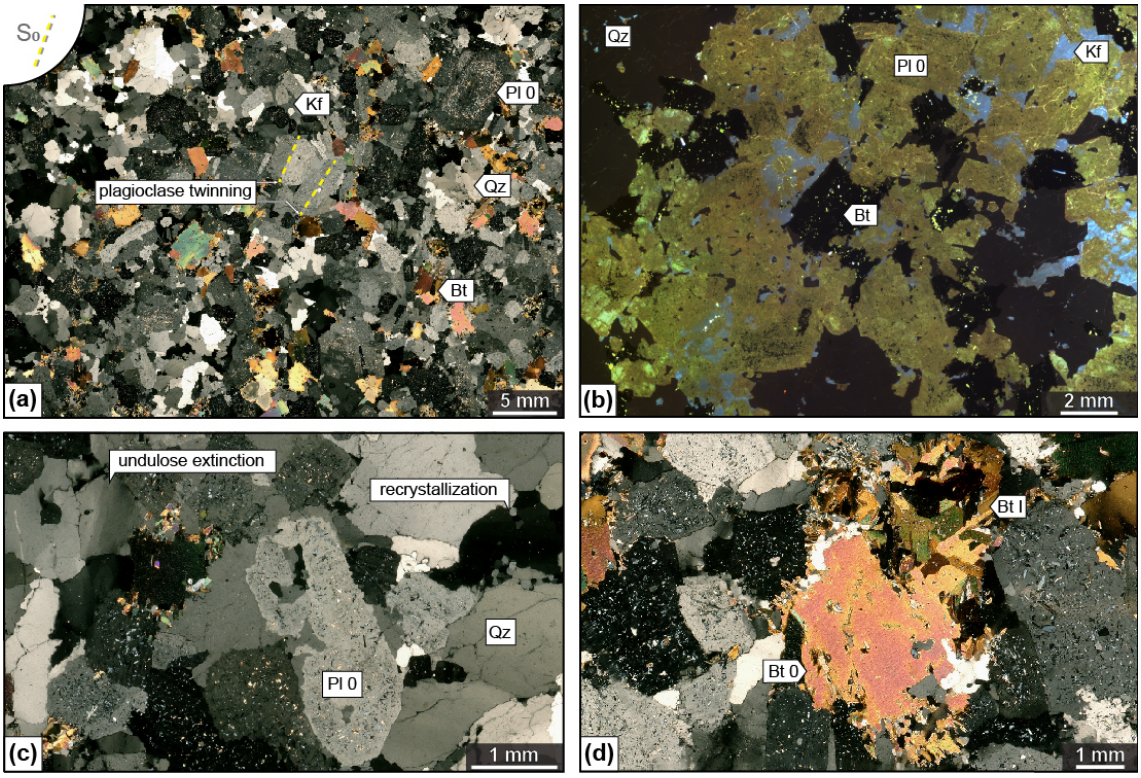

Figure 2: *(2-column fitting image)* Mineralogy and microstructure of the Neves metagranodiorite (13NEV01A). (a) Cross-polarized photomicrograph of the thin section. The magmatic foliation S_0 is highlighted by the aligned twin planes in plagioclase (the yellow dashed lines). (b) Cathodoluminescence (CL) picture. Quartz (Qz): dark blue, plagioclase (Pl_0: greenish, potassic feldspar (Kf): light blue, biotite (Bt): dark. (c) Quartz microstructures. (d) Recrystallization of magmatic biotite (Bt_0 in new metamorphic grains (Bt_2). Mineral abbreviations are from Whitney and Evans (2010)

.

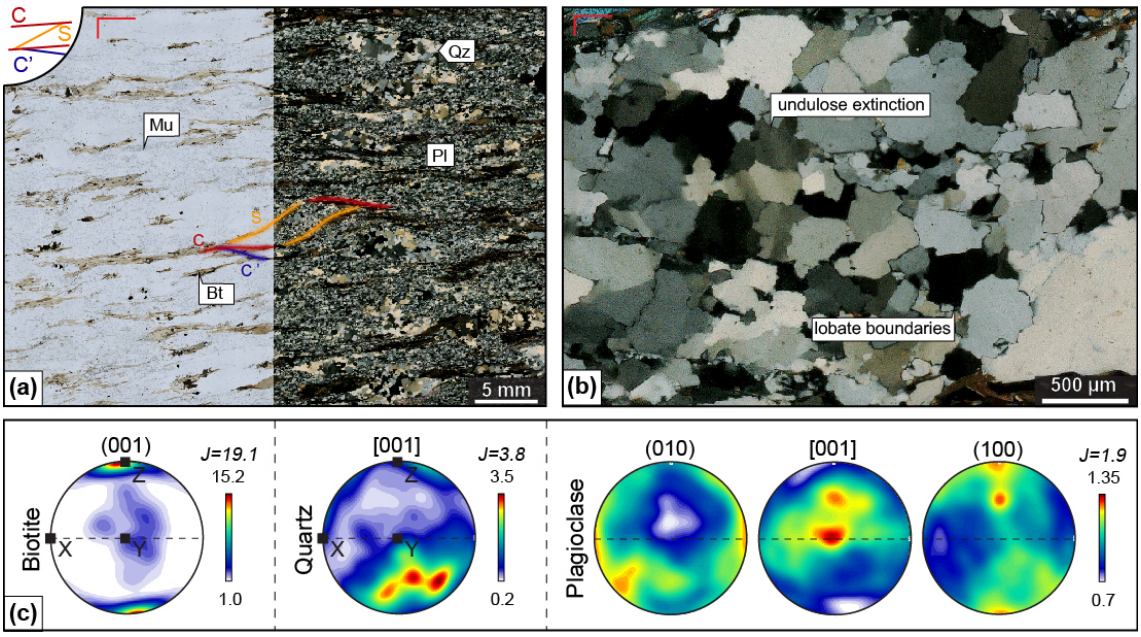

Figure 3: *(2-column fitting image)* Mineralogy and microtextures of protomylonite 2 (18NEV01B) (a) Plane-polarized (left) and cross-polarized (right) photomicrographs of the thin section. The sigmoid highlights the C-, S- and C'-planes, in red, orange and blue, respectively. (b) Quartz microstructures. (c) CPO of quartz, plagioclase and biotite (lower hemisphere).

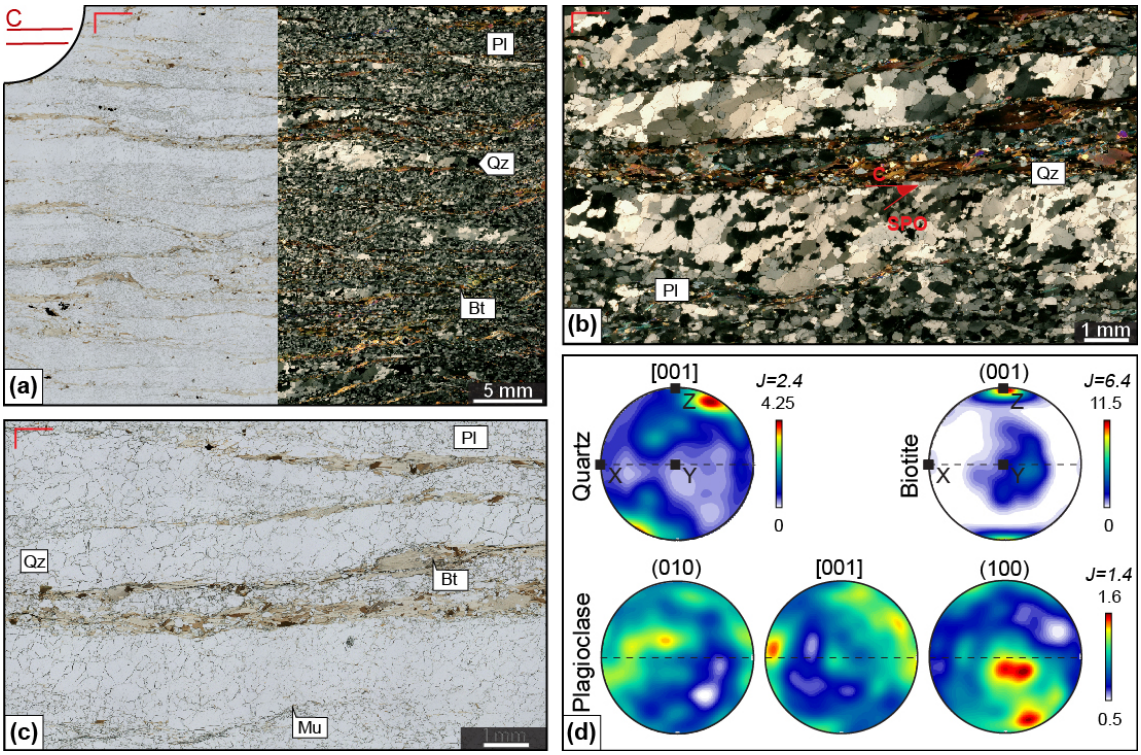

Figure 4: *(2-column fitting image)* Mineralogy and microtextures of the mylonite (13NEV01C) (a) Plane-polarized (left) and cross-polarized (right) photomicrographs of the thin section. (b-c) Metamorphic layering defined by the alternance of quartz, plagioclase, and micas ribons. Shape-preffered orientation (SPO) of quartz at ∼35° from the C-plane is highlighted on (b). (d) CPO of quartz, plagioclase and biotite (lower hemisphere).

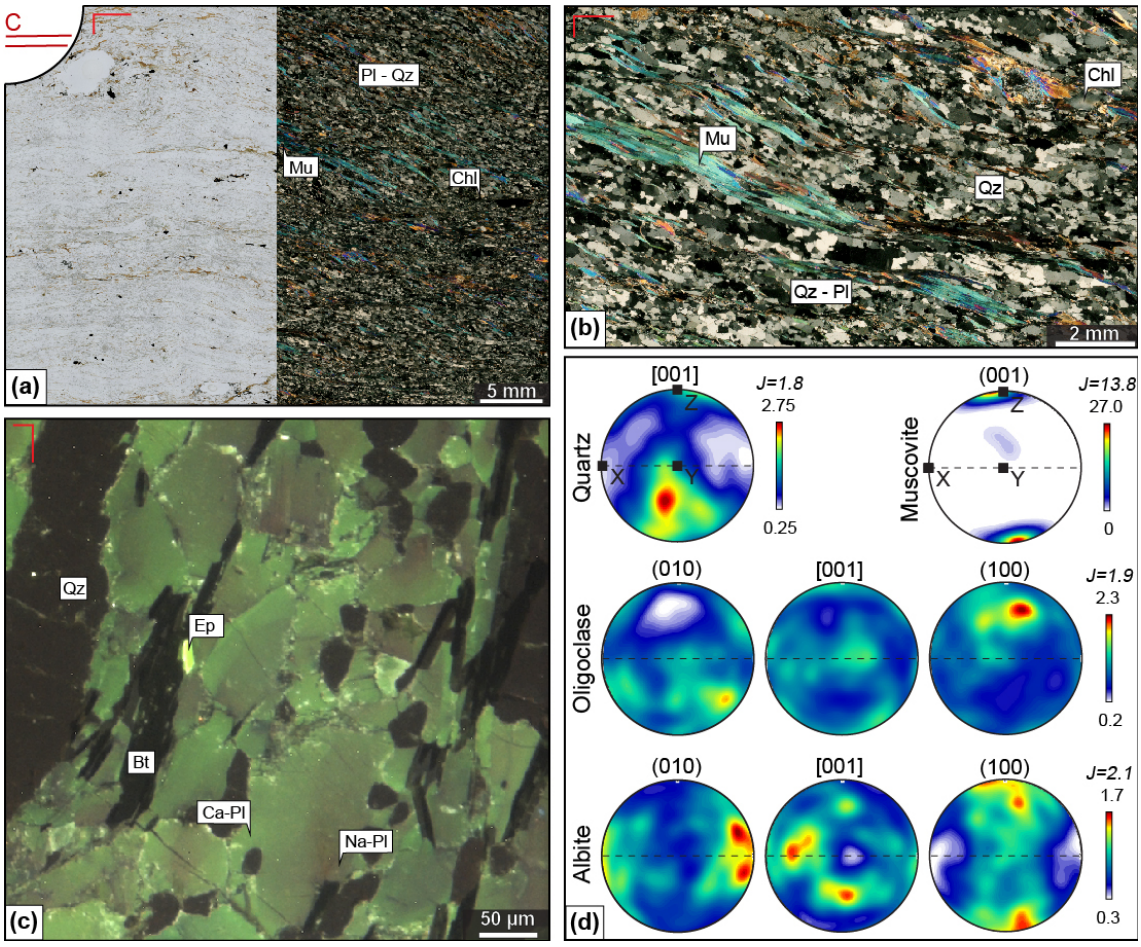

Figure 5: *(2-column fitting image)* Mineralogy and microtextures of the utramylonite (13NEV01D) (a) Plane-polarized (left) and cross-polarized (right) photomicrographs of the thin section. (b-c) Intense metamorphic layering defined by the alternance of muscovite ribbons and mixed plagioclase-quarz domains. (c) CL imaging highlighting the two populations of plagioclase, CL colors traducing the Na-Ca ratio (Na-rich: reddish, Ca-rich: greenish).(d) CPO of quartz, muscovite, Ca-rich (oligoclase) and Na-rich (albite) plagioclase (lower hemisphere).

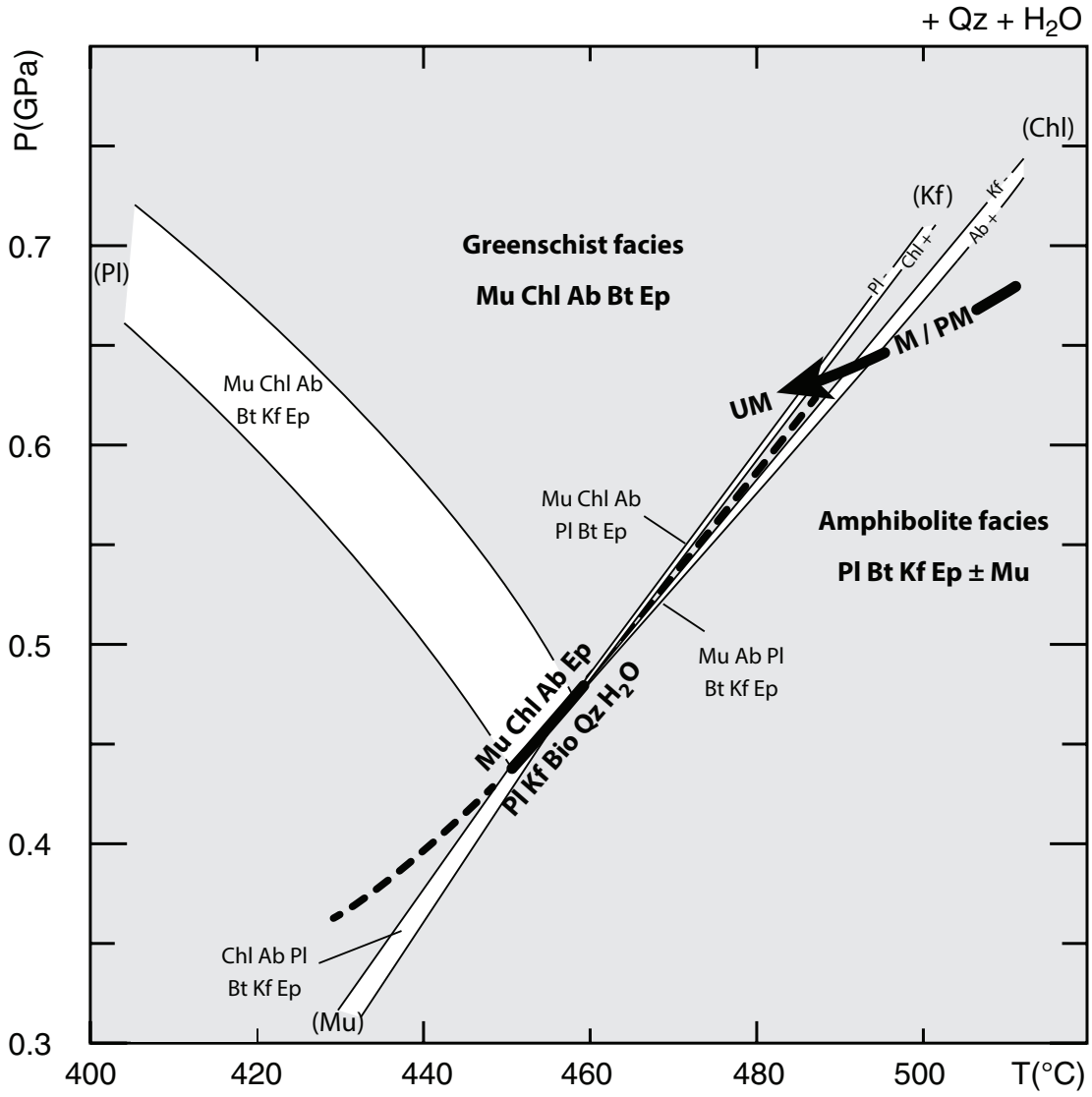

Figure 6: *(1-column fitting image)* Pressure-temperature conditions of deformation. P-T phase diagram section computed in the NaCaKFMASH system from the bulk chemical composition of the Neves metagranodiorite 13NEV01A (SiO_2 71.43 : Al_2O3 11.05 : FeO 4.31 : MgO 1.97 : CaO 4.99 : Na_2O 4.79 : K_2O 1.46, in mol %). Divariant equilibria (in white) are named with the missing phase in parenthesis. The black arrow materializes the evolution of the metamorphic conditions during deformation, from the amphibolite-facies deformation related to protomylonites (PM) and mylonite (M) (high-temperature field ¿ 500 °C, where Bt, Pl and Kf are stable), to the greenschist-facies ultramylonite (UM, lower-temperature field 450-500 °C, where Mu, Ab and Chl are stable). The transition between the two fields is the univariant reaction represented by the thick black line. The thick dashed line corresponds to the metastable extension of this reaction.

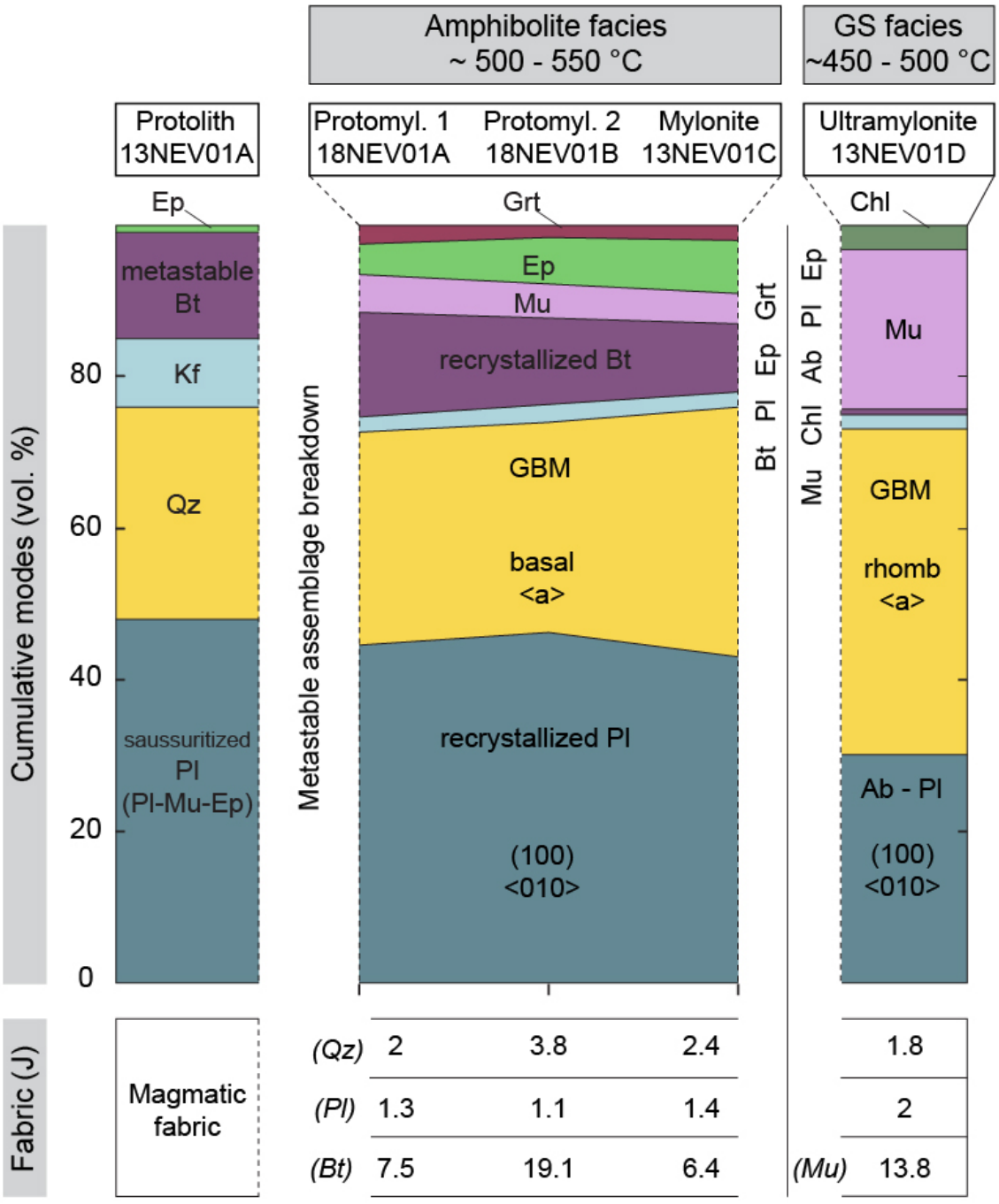

Figure 7: *(1-column fitting image)* Evolution of cumulative modes and fabrics with strain. The color coding refers to that of the phase maps obtained by EBSD (see Supplementary Material S7).

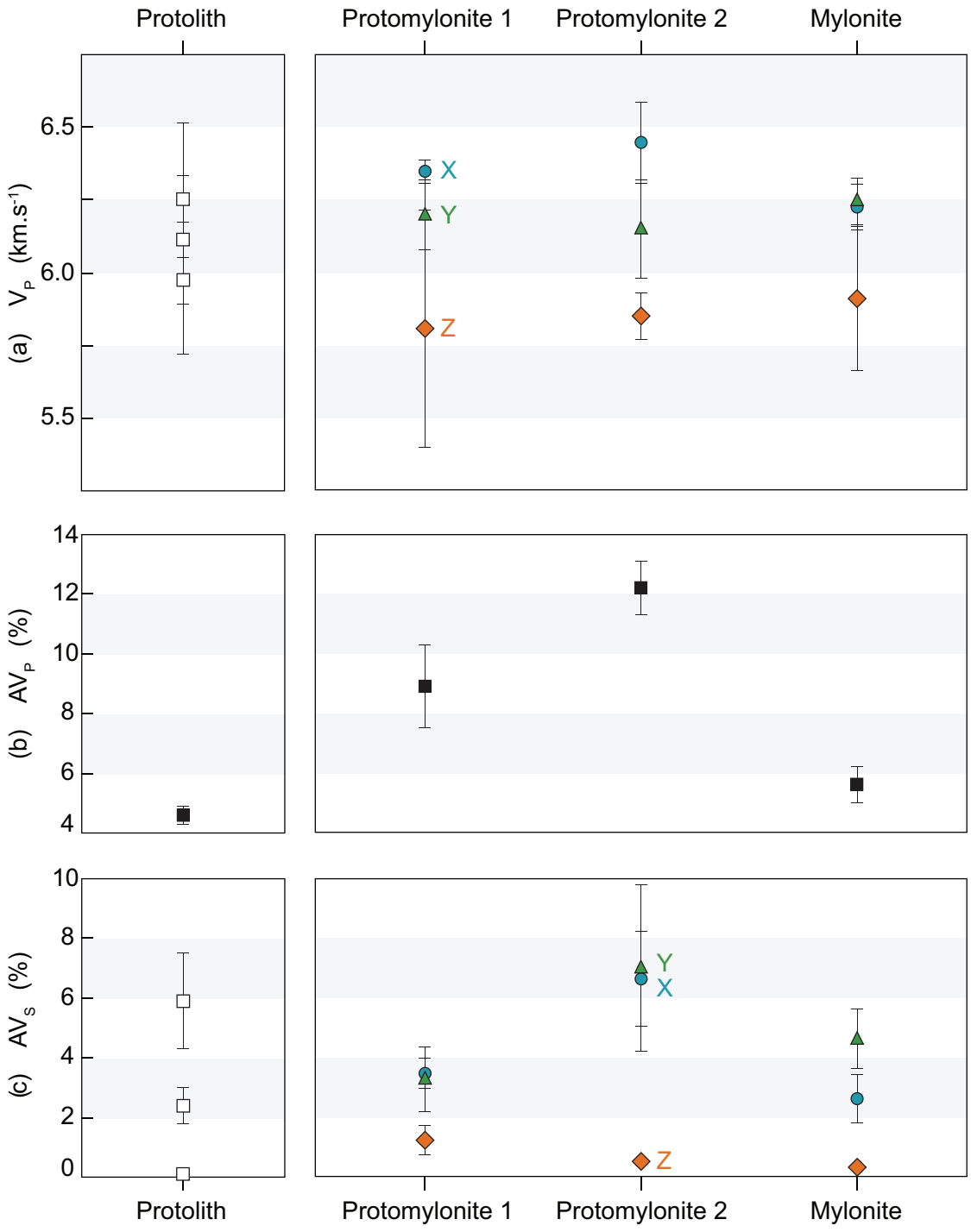

Figure 8: *(2-column fitting image)* Measured V_P (a), AV_P (b) and AV_S (c). The white squares are the results obtained in the protolith, along undifferentiate directions. Blue circles, green triangles and orange diamonds are the results obtained along the X-, Y- and Z-axes of the strain ellipsoid, respectively, in the deformed samples. There are no data for the ultramylonite.

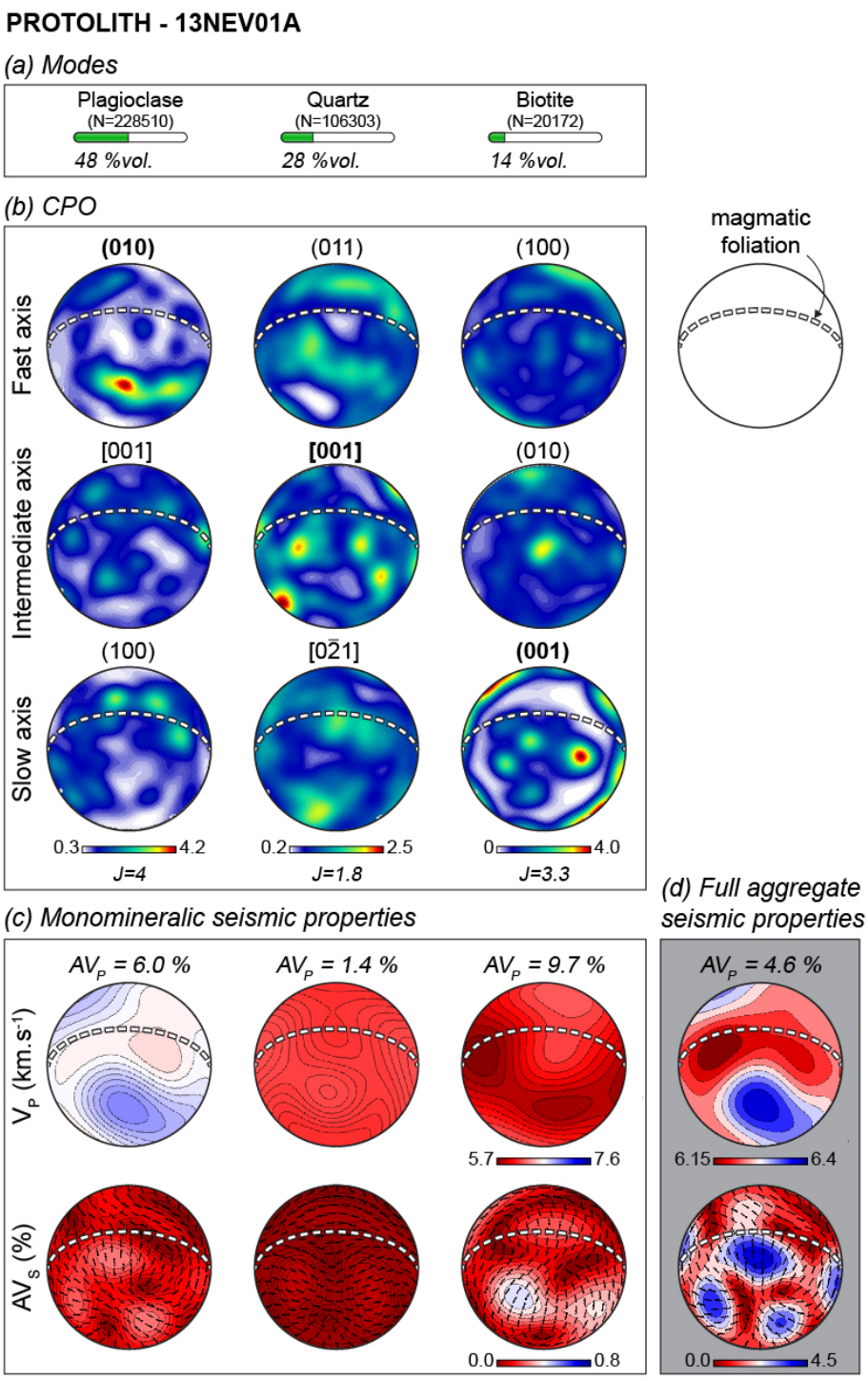

Figure 9: *(2-column fitting image)* Texture and calculated seismic properties of the protolith 13NEV01A. The dashed white line materializes the magmatic foliation. (a) Modal proportions of the main mineral phases. N is the number of points measured by EBSD. (b) CPO. For each phase, CPO is expressed for the fastest, intermediate and slowest P-wave propagation axes. Phases are ranked by descending order of abundance. Axes in bold font are the main axes described in the text. (c) Calculated seismic properties (V_P, AV_P and AV_S) of the monocrystalline aggregates. Stereographic normalized plots represent the spatial distributions of V_P (top) and AV_S (bottom). (d) Calculated seismic properties of the whole rock aggregate.

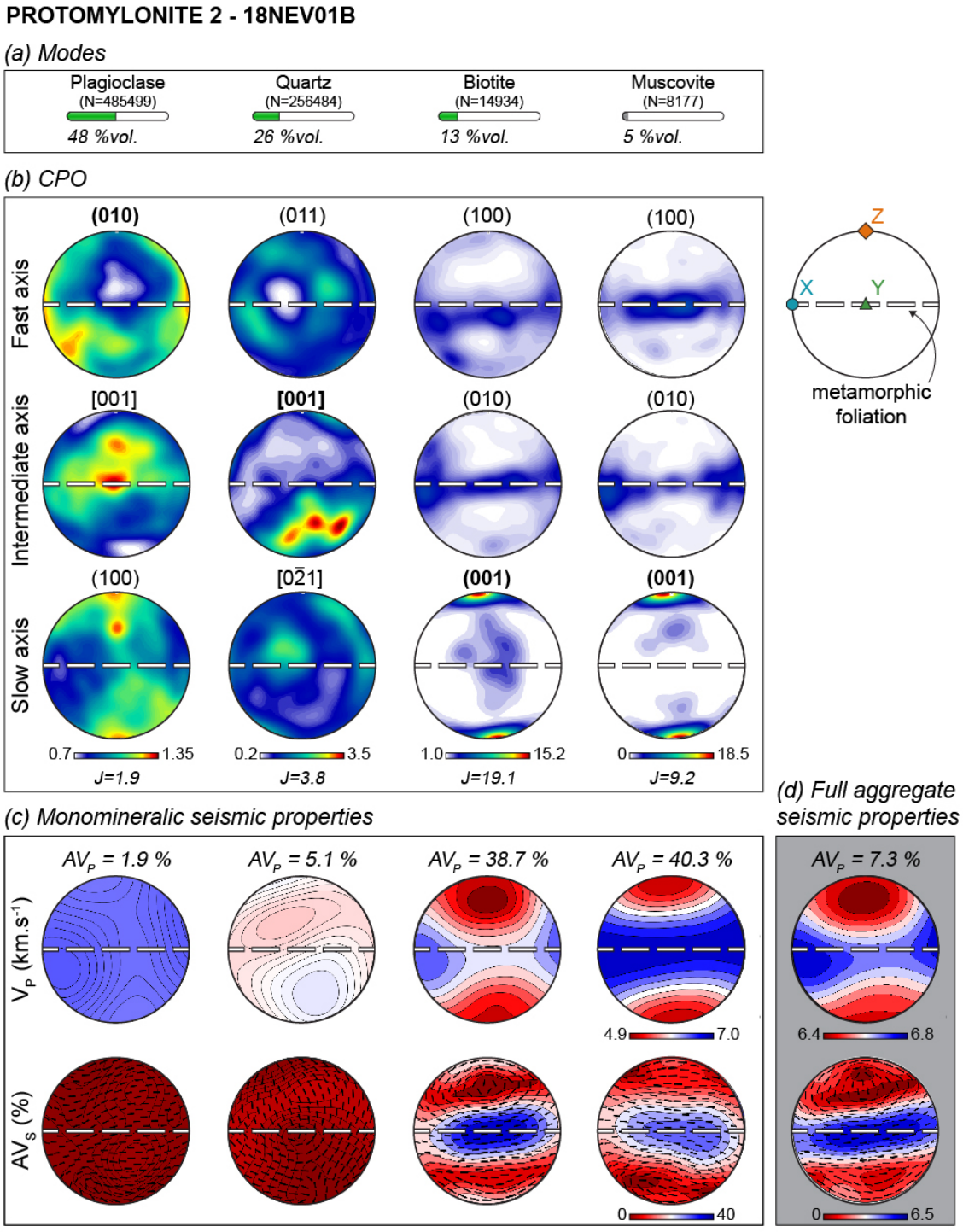

Figure 10: *(2-column fitting image)* Texture and calculated seismic properties of protomylonite 2 18NEV01B. (a) Modal proportions of the main mineral phases. N is the number of points measured by EBSD. (b) CPO. For each phase, CPO is expressed for the fastest, intermediate and slowest P-wave propagation axes. Phases are ranked by descending order of abundance. Axes in bold font are the main axes described in the text. (c) Calculated seismic properties (V_P, AV_P and AV_S) of the monocrystalline aggregates. Stereographic normalized plots represent the spatial distributions of V_P (top) and AV_S (bottom). (d) Calculated seismic properties of the whole rock aggregate.

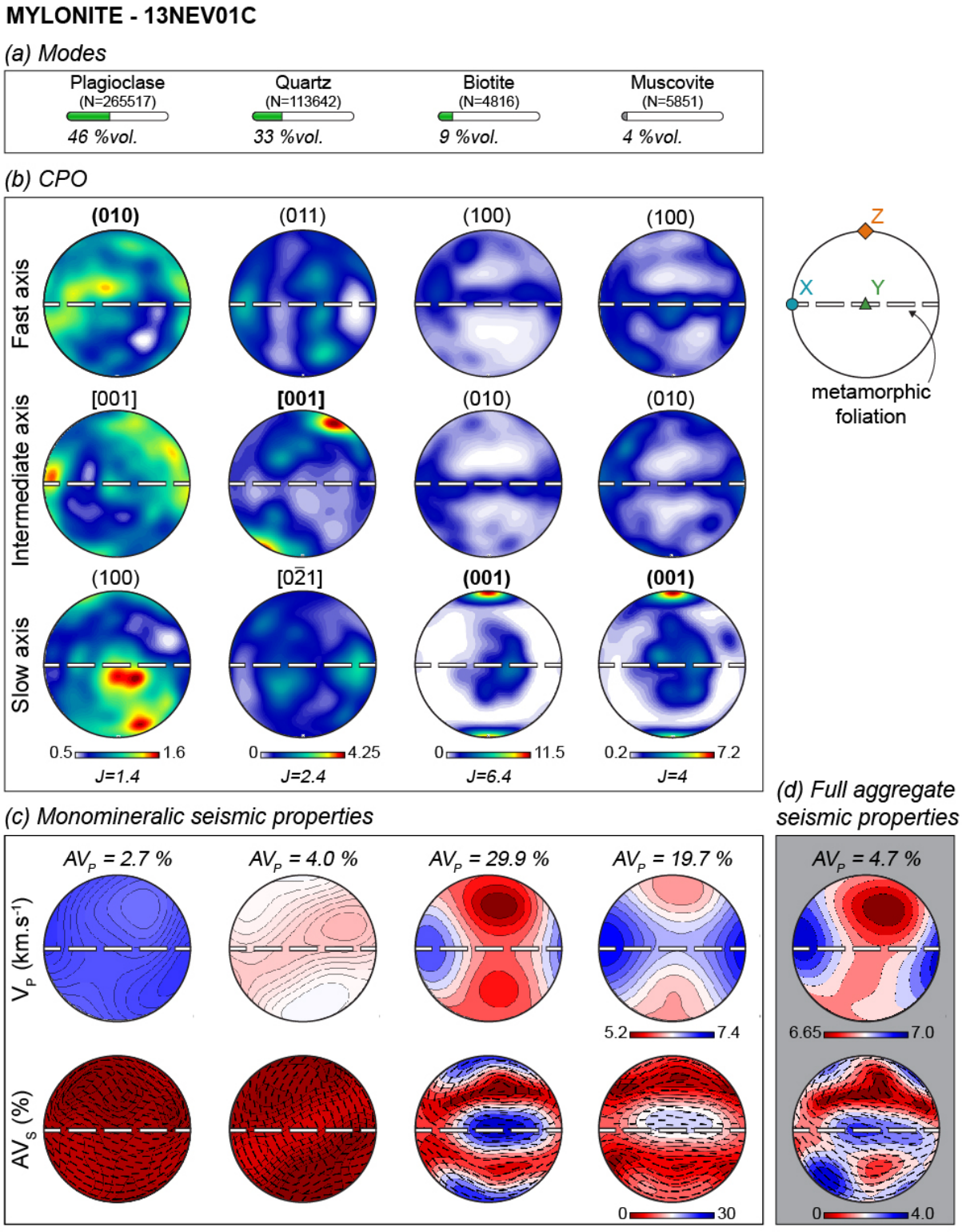

Figure 11: *(2-column fitting image)* Texture and calculated seismic properties of the mylonite 13NEV01C. (a) Modal proportions of the main mineral phases. N is the number of points measured by EBSD. (b) CPO. For each phase, CPO is expressed for the fastest, intermediate and slowest P-wave propagation axes. Phases are ranked by descending order of abundance. Axes in bold font are the main axes described in the text. (c) Calculated seismic properties (V_P, AV_P and AV_S) of the monocrystalline aggregates. Stereographic normalized plots represent the spatial distributions of V_P

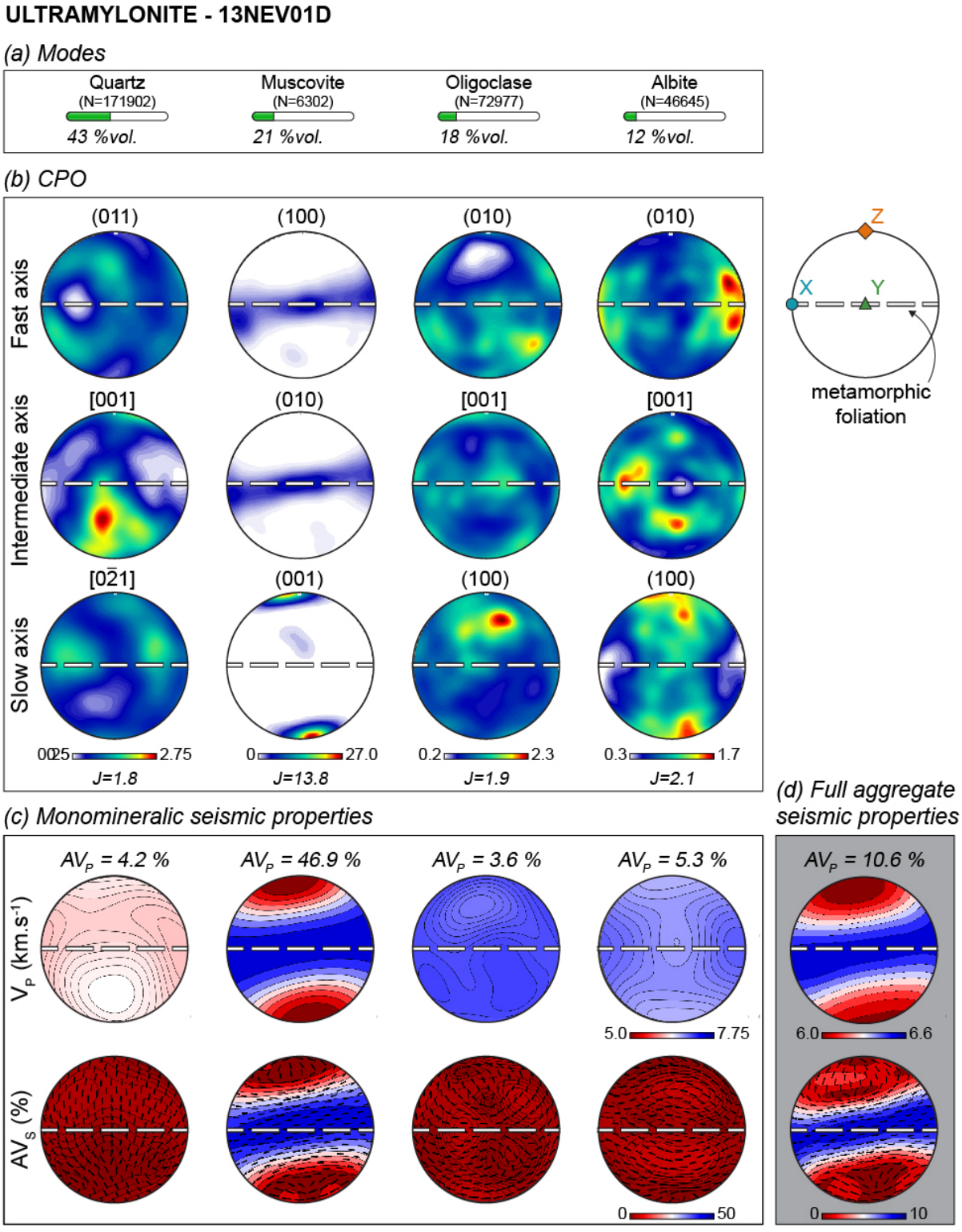

Figure 12: *(2-column fitting image)* Texture and calculated seismic properties of the ultramylonite 13NEV01D. (a) Modal proportions of the main mineral phases. N is the number of points measured by EBSD. (b) CPO. For each phase, CPO is expressed for the fastest, intermediate and slowest P-wave propagation axes. Phases are ranked by descending order of abundance. Axes in bold font are the main axes described in the text. (c) Calculated seismic properties (V_P, AV_P and AV_S) of the monocrystalline aggregates. Stereographic normalized plots represent the spatial distributions of

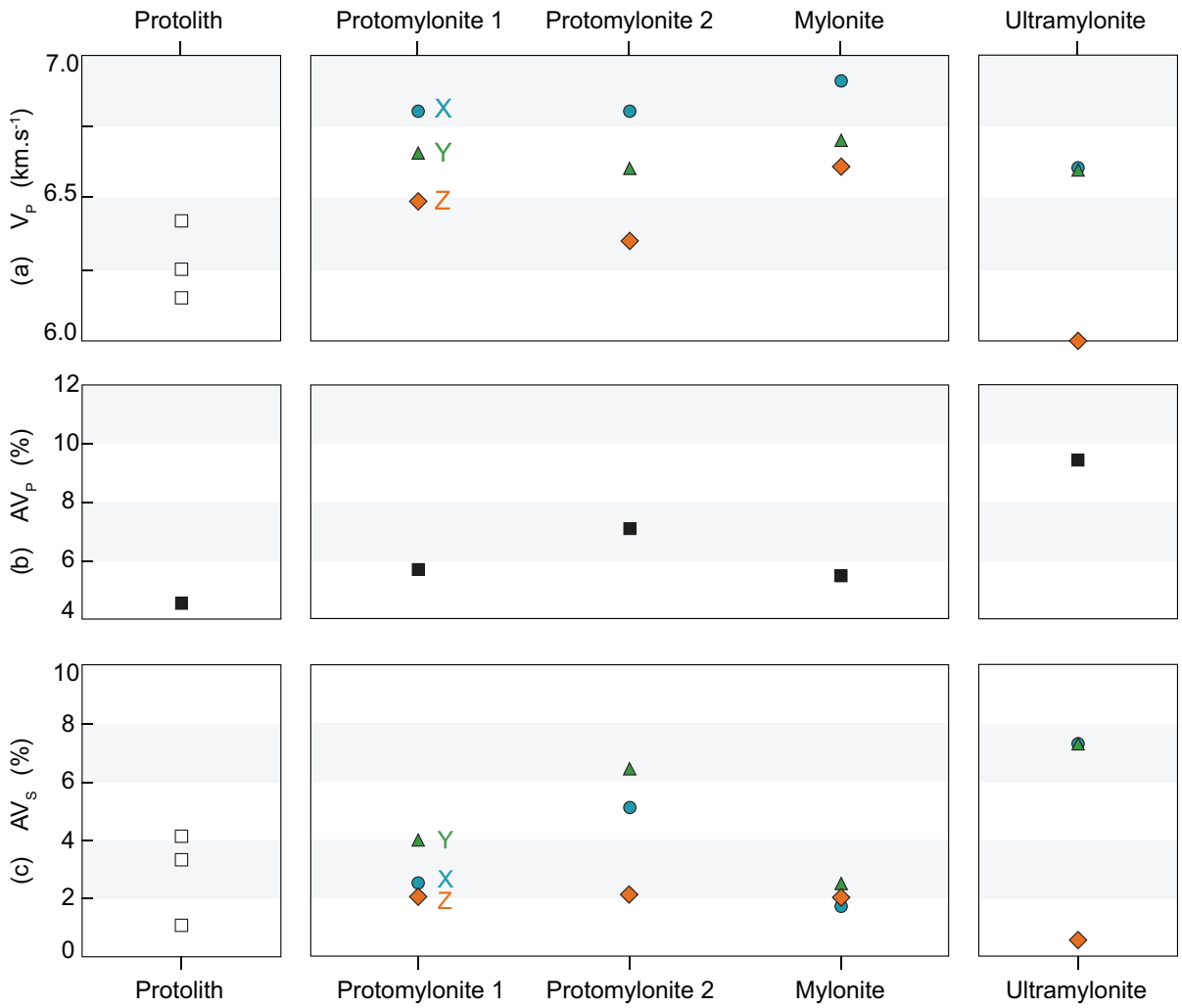

Figure 13: *(2-column fitting image)* Calculated V_P (a), AV_P (b) and AV_S (c). The white squares are the results obtained in the protolith, along undifferentiate directions. Blue circles, green triangles and orange diamonds are the results obtained along the X-, Y- and Z-axes of the strain ellipsoid, respectively, in the deformed samples.

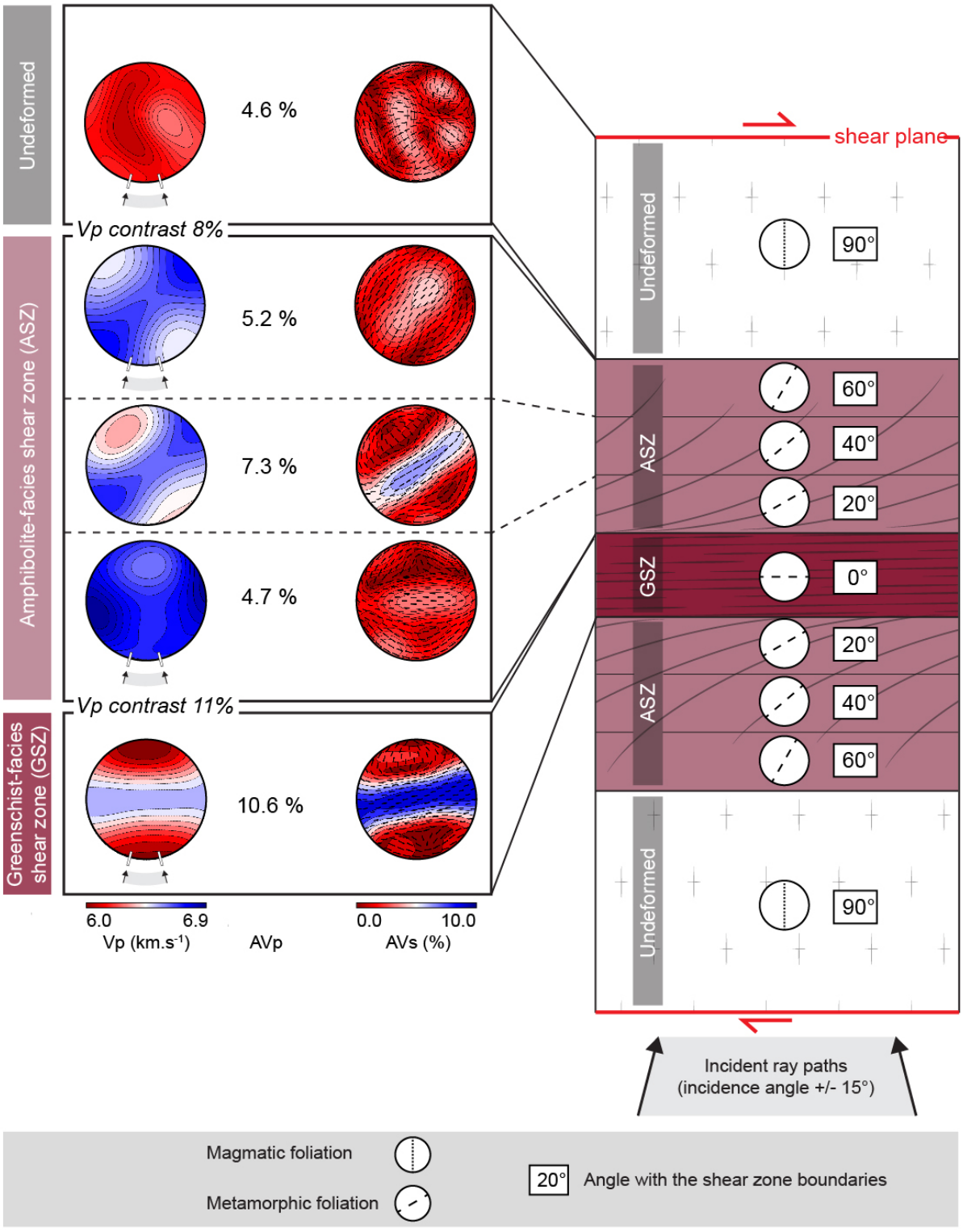

Figure 14: *(2-column fitting image)* Simplified model of the dextral meter-scale shear zone. On the right, the circular plots and the angle value represent the orientation of the magmatic/metamorphic foliation. On the left, the pole figures represent the normalized spatial distributions of V_P and AV_S for each stage, which have been rotated following the orientation of the foliation. AV_P is indicated in percent. Teleseismic P-waves propagating through the horizontal shear zone are represented below the model and the circular plots, as a cone of incident ray paths at 15° on either side of the

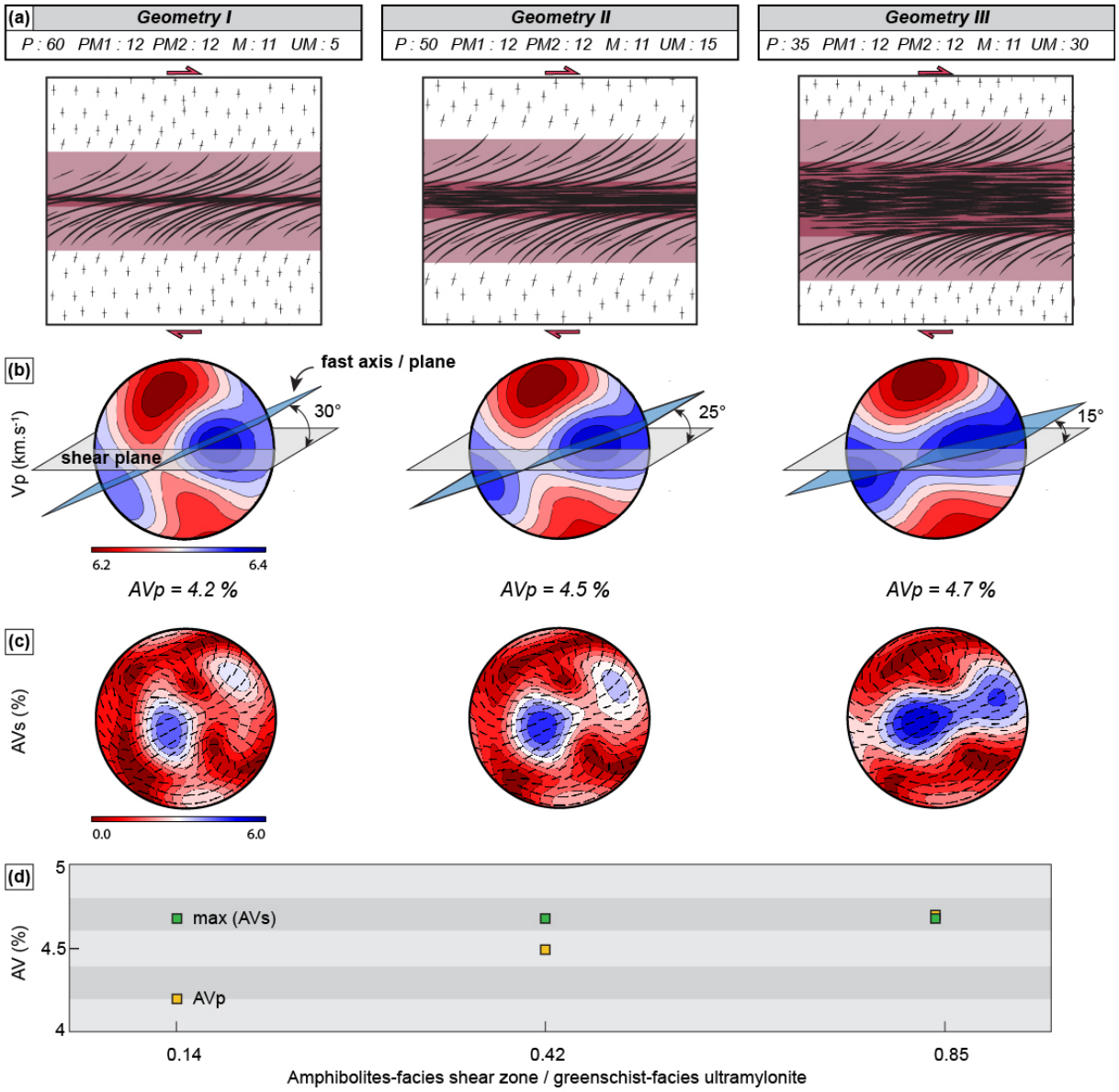

Figure 15: *(2-column fitting image)* Calculated seismic properties of a whole shear zone. (a) Relative proportions of the protolith, the amphibolite-facies marginal zone and the greenschist-facies ultramylonite zone of the three modelled geometries, illustrated in the cartoons. (b) Spatial distributions of V_P. The angle between the C-plane and the fast P-wave propagation plane is represented. (c) Spatial distributions of AV_S. (d) Evolution of AV_P and $AV_S(max)$ with the amphibolite versus greenschist shear zone ratio.

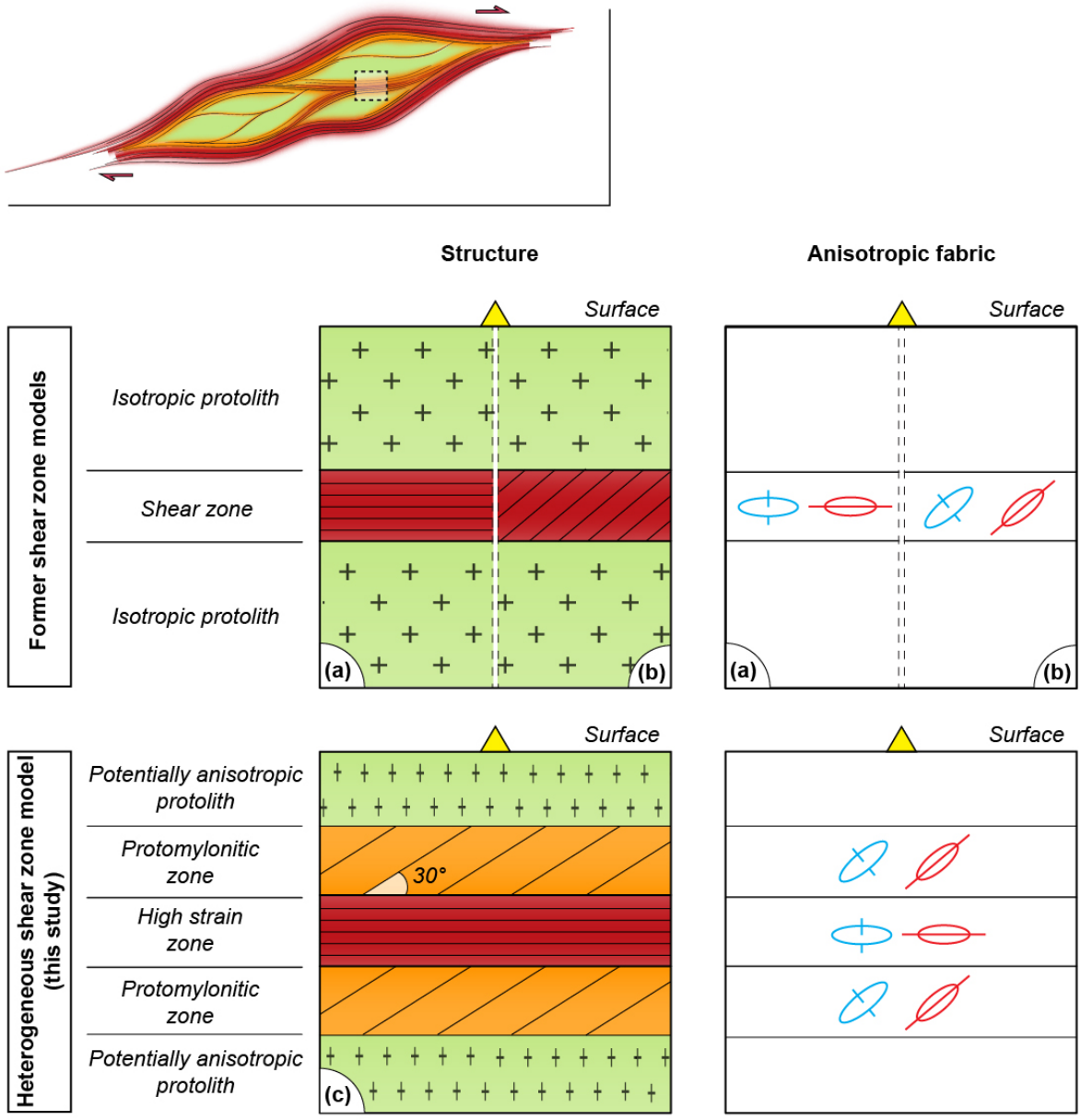

Figure 16: *(1.5-column fitting image)* Model of spatial variabilityof the seismic properties across a crustal shear zone. (a-b) Former geophysical models for shear zones, consisting in an homogeneous anisotropic layer with the fast plane (a) parallel (e.g. Schulte-Pelkum & Mahan, 2014) or (b) oblique (e.g. Schulte-Pelkum et al., 2005; Zandt et al., 2004) to shear zone boundaries. (c) New model (this study), taking both into account the oblique fabric of the marginal zone with an orthorhombic symmetry and the parallelized fabric of the ultramylonite zone with a hexagonal symmetry. Left-side cartoons represent the structure of the models, right-side cartoons, the orientation of the anisotropic fabric.

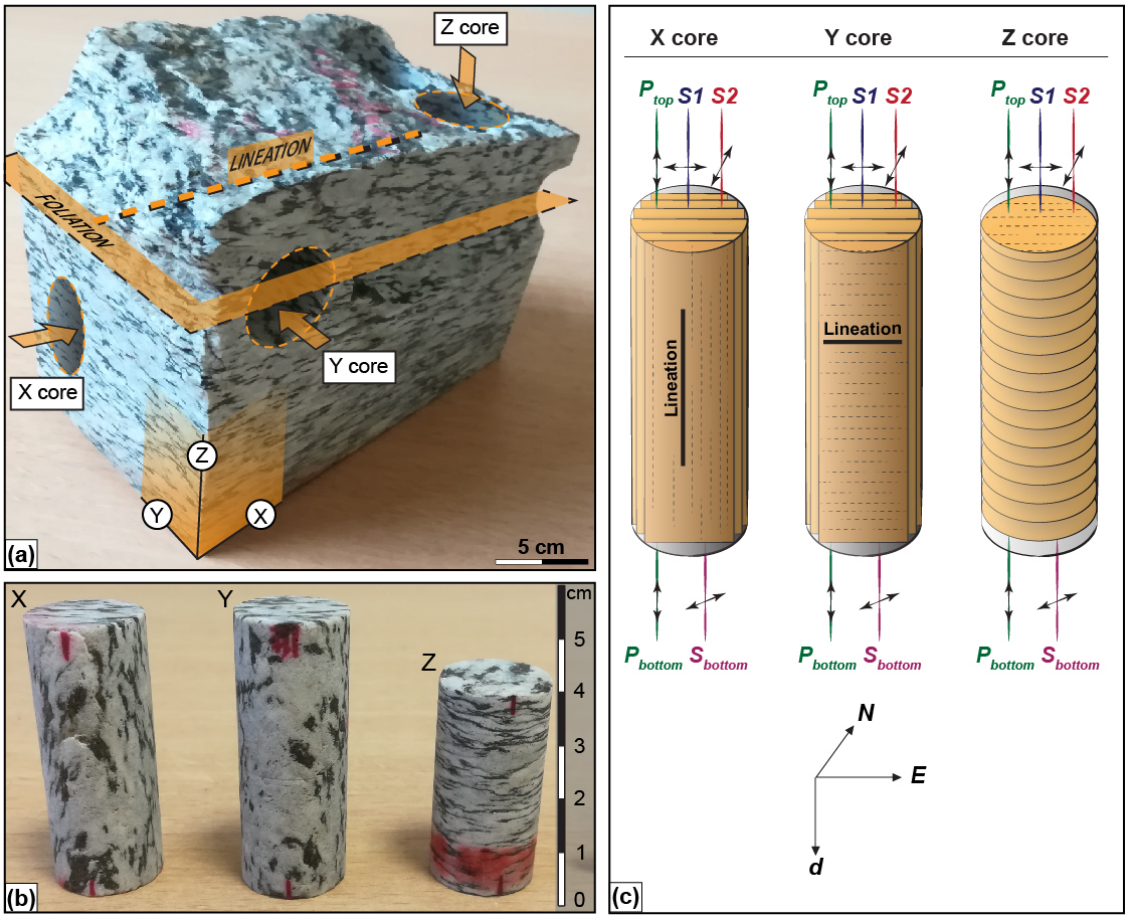

Figure 17: *(2-column fitting image)* (a) Drilling directions within a homogeneously deformed sample : X (along the lineation), Y (parallel to the foliation and perpendicular to the lineation) and Z (normal to the foliation). (b) The three cores, X, Y and Z. (c) Orientation of the ductile structure in the X, Y and Z cores, and its position with respect to the polarization of the piezoelectric transducers. The orange plane is the foliation plane, the dashed line is the lineation. Acoustic wave are emitted by P_{bottom} and S_{bottom} and received by P_{top}, S_1 and S_2. The P_{bottom} ans P_{top} transducers are both polarized along d (depth). The S_{bottom}, S_1 and S_2 transducers are polarized towards N45°E, E (East) and N (North), respectively.

S2. Pulsed-receiver settings

Receiver	
Bandwidth (MHz)	35
Gain (dB)	10
High pass filter	Out
Low pass filter	35
Pulser	
Type	DPR300
Trigger	Internal
Damping (Ohms)	331
Energy	4
PRF (kHz)	100
Echo/Through mode	Through
Voltage (V)	207
Impedance	High

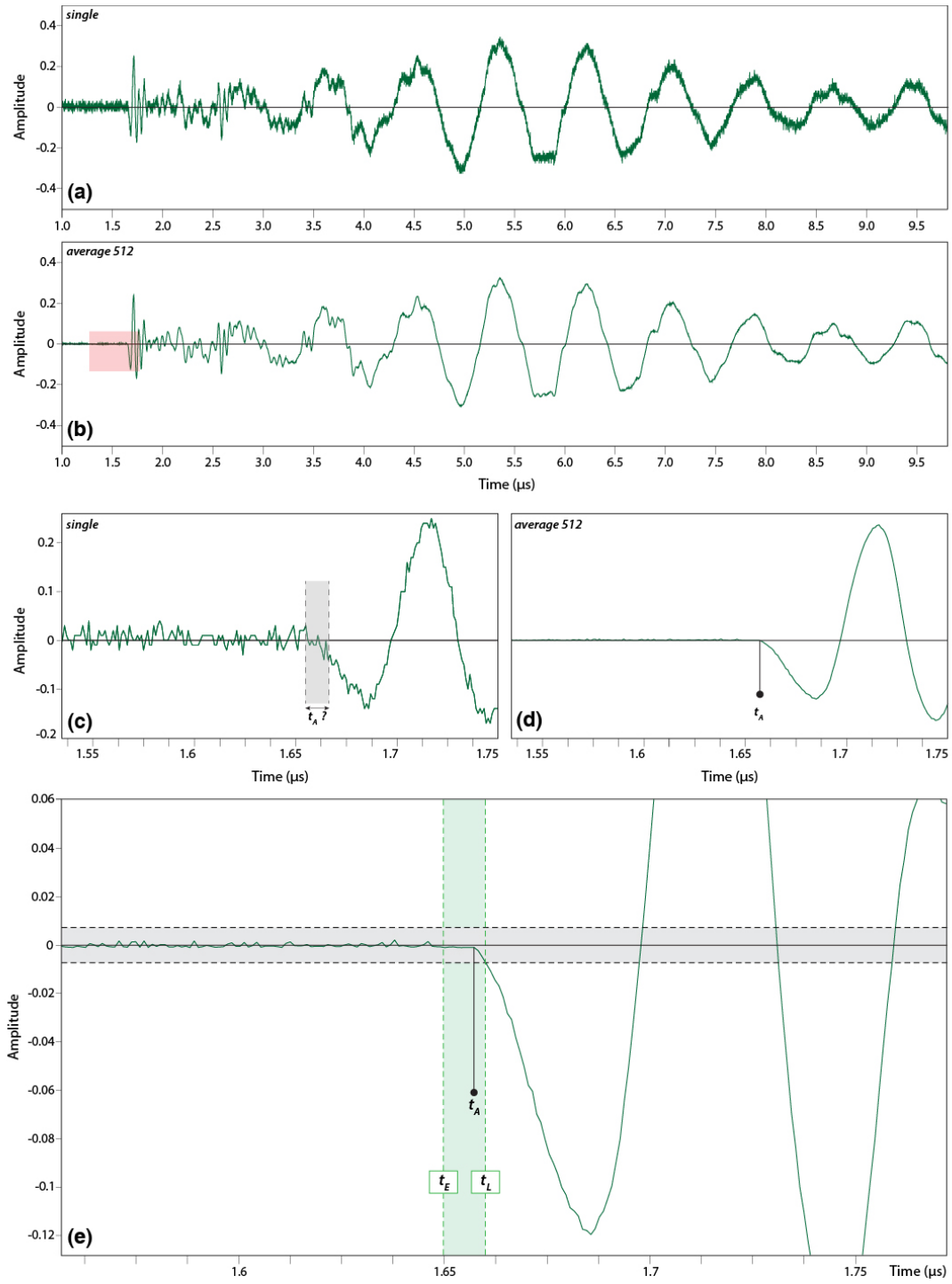

Figure 18: S2. (a-d) Effect of the acquisition method on the signal-to-noise ratio (case of a P wave propagating through a mylonite sample). (a-c) "Single" mode: signal obtained from a single electric pulse. (b-d) "Average" mode: average of the signals generated by 512 eletric pulses. (c) and (d) are zooms of (a) and (b), respectively, near the seismci phase arrival. The red square is the location of the time window used in for the picking of the seismic phase arrival. (e) Picking method. The dashed black lines are the ASNR (Amplitude-based Signal-to-Noise Ratio) thresholds, defining a grey band in which the earliest (t_E), latest (t_L and most likely (t_A) arrival times are picked. t_E is the last point with a null derivative, t_L is the intersection between the signal and the ASNR threshold. t_A is picked within this time window, at the basis of the first inflection.

S4. Analytical settings of EBSD mapping

Sample	13NEV01A	18NEV01A	18NEV01B	13NEV01C	13NEV01D
Resolution (width) (px)	908	1009	1357	955	532
Resolution (height) (px)	682	695	849	752	750
Step size (µm)	33.3	10.6	12.4	10.1	10.6
Field width (mm)	30.2	10.7	16.8	9.62	5.64
Field height (mm)	22.7	7.37	10.5	7.57	7.95
Number of points	619256	701255	1152093	718160	399000
Hit rate (%)	70.1	77.0	79.8	67.1	78.3
Accelerating voltage (kV)			15.00		
Working distance (mm)	27.3	23.7	21.1	16.7	14.7
Detector insertion distance (mm)	169.1	169.1			
Reanalysis time (h:mn:s)	00:10:16	00:08:54	00:18:07	00:11:05	00:06:00
Speed of reanalysis (Hz)	782.8	1091.9	922.8	980.4	1064.2
Specimen tilt (°)			0		
EBSD camera binning mode (px x px)			336x256		
EBSD camera exposure time (ms)	11.7	5.1	3.0	4.6	2.6
EBSD camera gain			1		
Static background correction			Activated		
Auto background correction			Activated		
Ban detection mode			Centers		
Number of bands detected			8		
Indexing mode			Optimized-TKD		

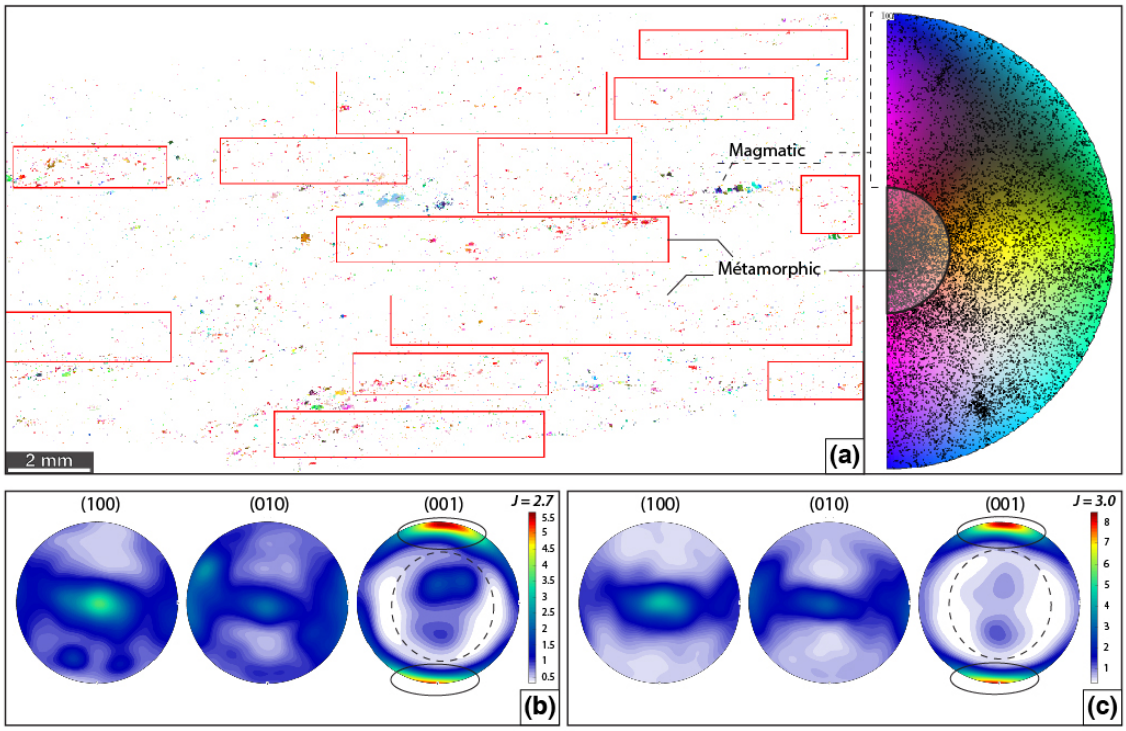

Figure 19: S4. Strategy for phyllosilicates nidexing by EBSD. (a) Selectiong of regions of interest on muscovite EBSD mapping. The legend on the right correspond to the inverse pole figure showing the Y axis (perpendicular to lineation) orientation in the muscovite crystal referential. CPO of (100), (010) and (001) of muscovite, before (b) and after (c) the selection of regions of interest.

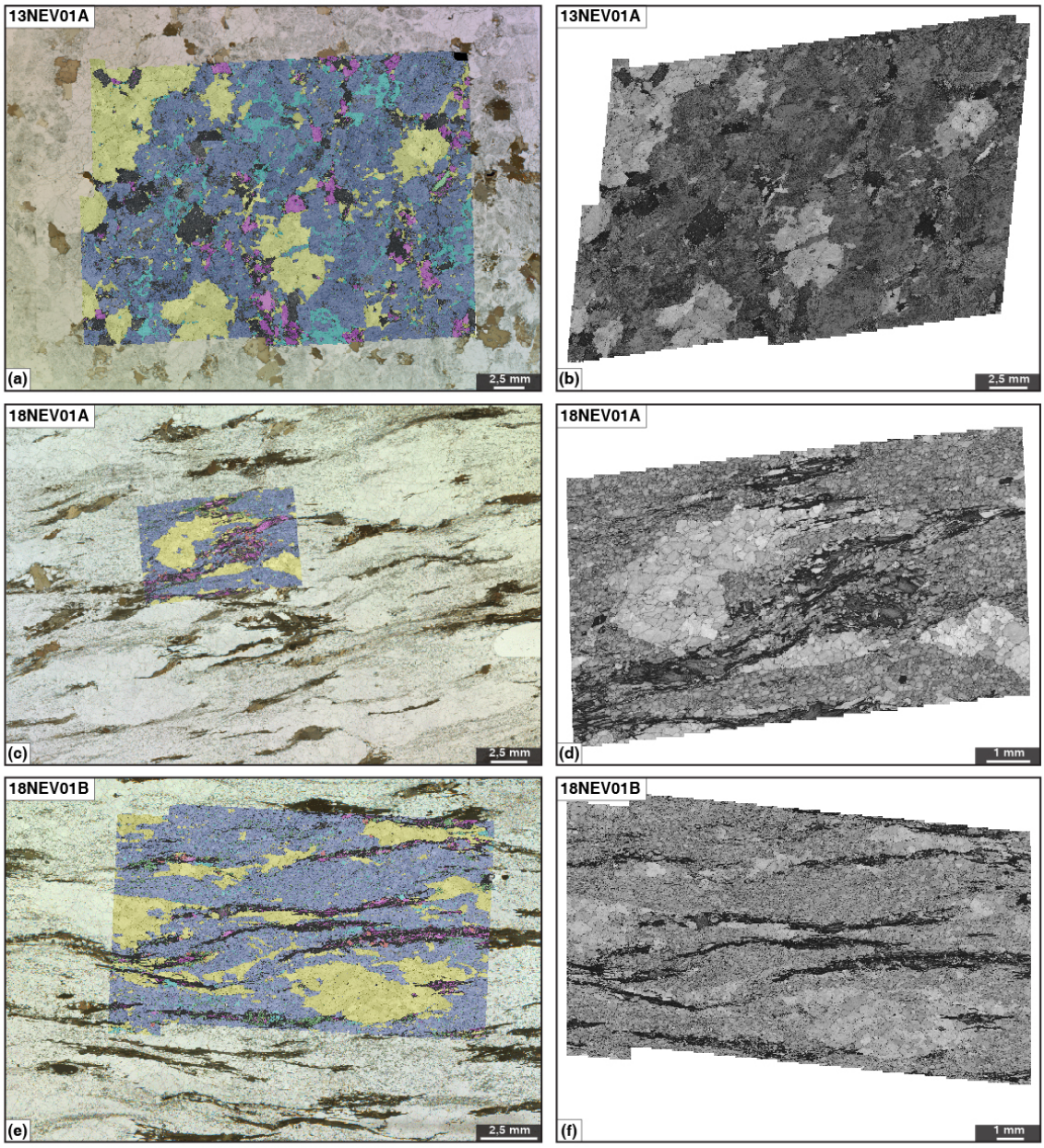

Figure 20: S5. Location of the EBSD map on the thin section (left) and Band contrast map (right) of the protolith 13NEV10A (a-b), protomylonite 1 18NEV01A (c-d), protomylonite 2 18NEV01B (e-f). Yellow: quartz, dark blue: plagioclase, light blue: K-feldspar, light purple: muscovite, dark purple: biotite, red: garnet, light green: epidote, dark green: chlorite.

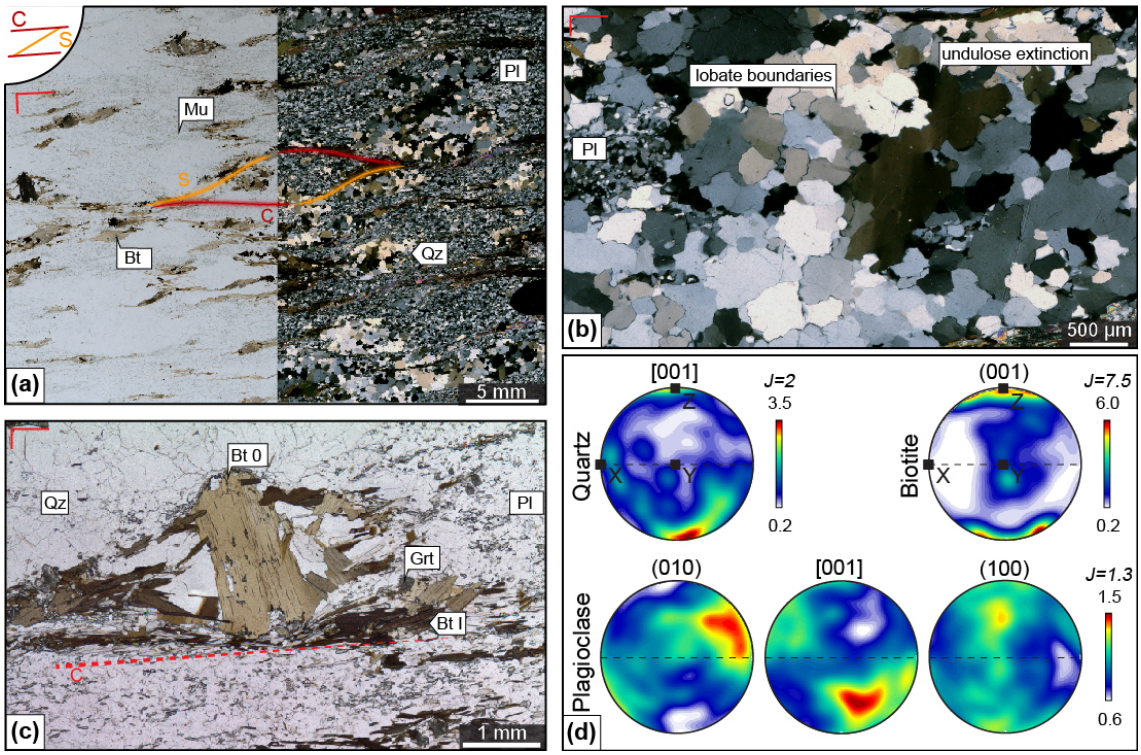

Figure 21: *(2-column fitting image)* Mineralogy and microtextures of protomylonite 1 (18NEV01A) (a) Plane-polarized (left) and cross-polarized (right) photomicrographs of the thin section. The sigmoid highlights the C- and S-planes, in red and orange, respectively. The red symbols indicate the orientation of X- (long) and Z- (short) axes. (b) Quartz microstructures. (c) Relict of Bt_0 preserved in a sigmoid defined by metamorphic Bt_1. Grt: garnet, Mu: muscovite. (d) CPO of quartz, plagioclase and biotite (lower hemisphere). Fabric strength is indicated by the J-index.

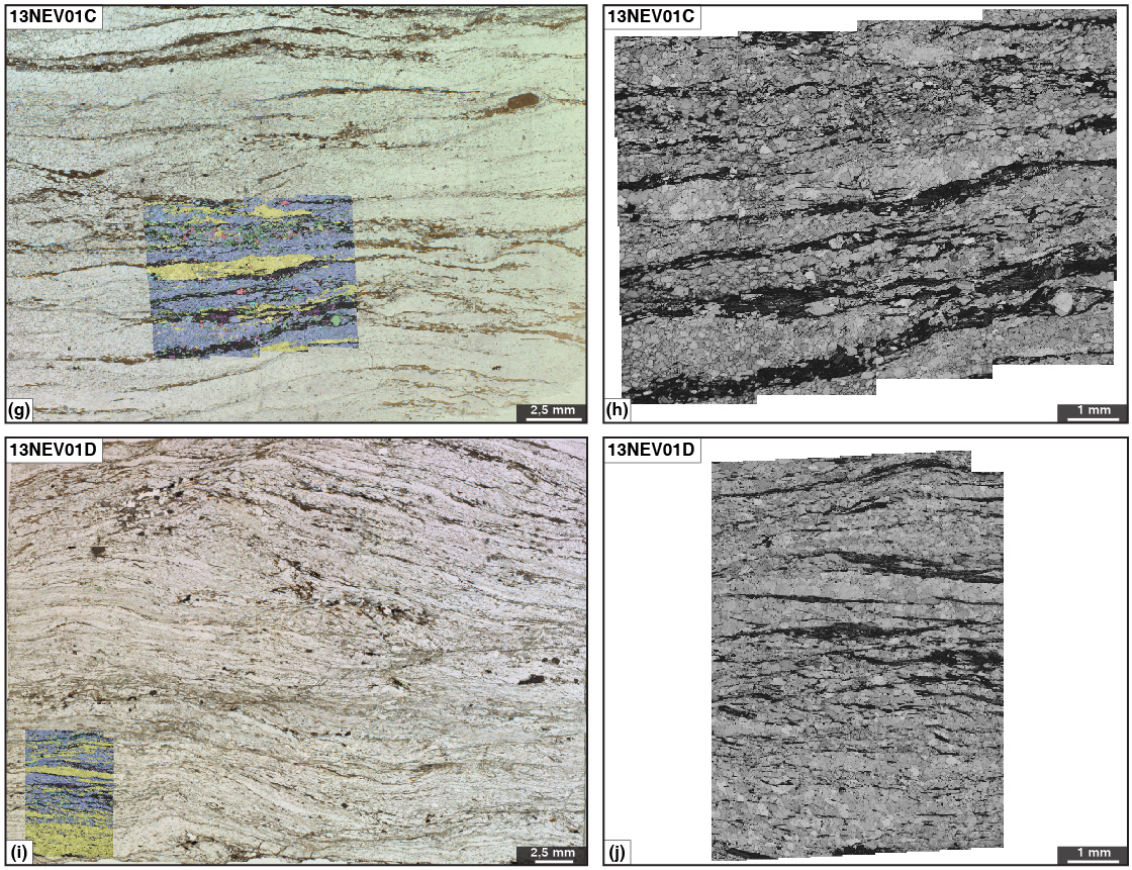

Figure 22: S5.(following) Location of the EBSD map on the thin section (left) and Band contrast map (right) of the mylonite 13NEV01C (g-h) and the ultramylonite 13NEV01D (i-j). Yellow: quartz, dark blue: plagioclase, light blue: K-feldspar, light purple: muscovite, dark purple: biotite, red: garnet, light green: epidote, dark green: chlorite.

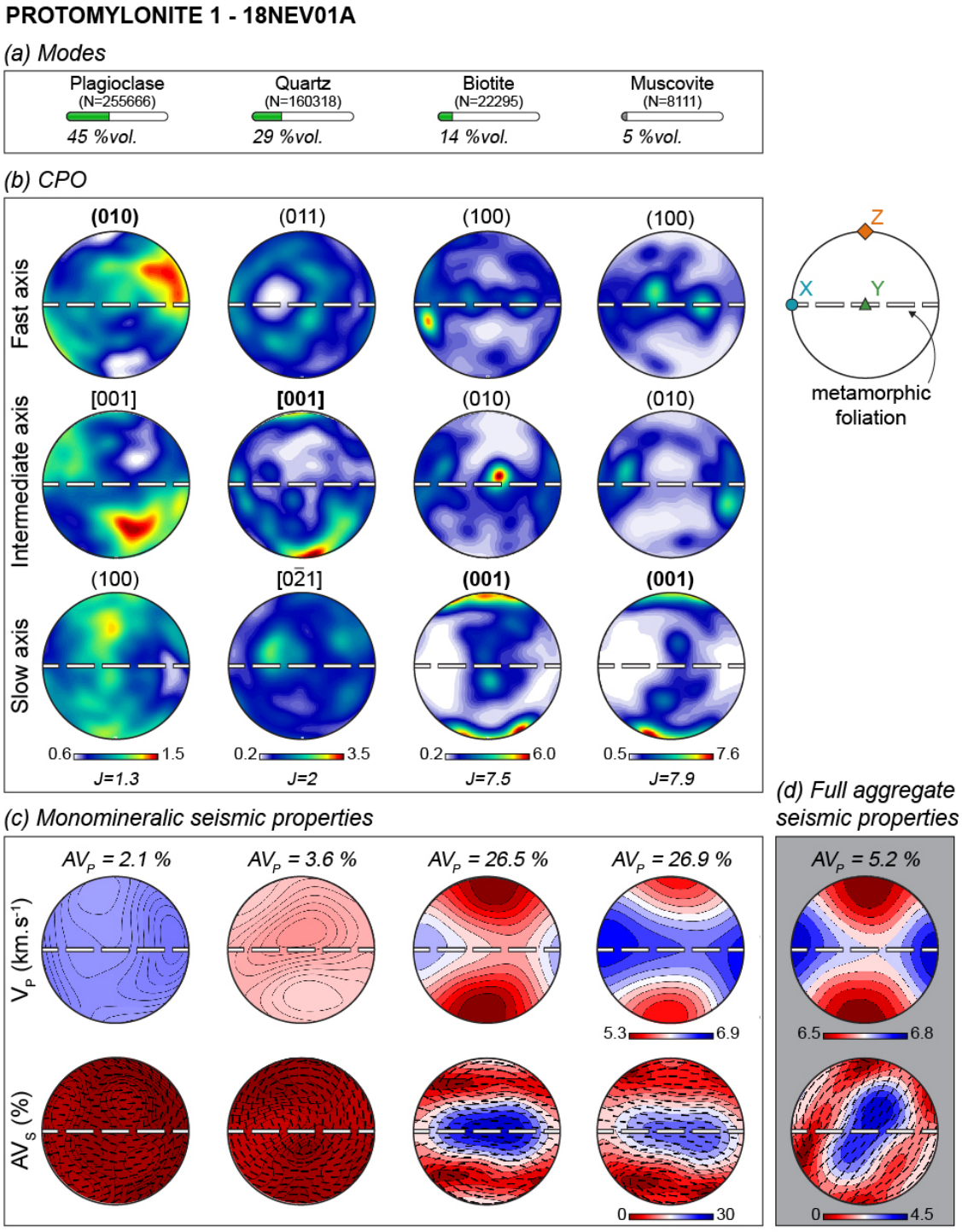

Figure 23: *(2-column fitting image)* Texture and calculated seismic properties of protomylonite 1 18NEV01A. (a) Modal proportions of the main mineral phases. N is the number of points measured by EBSD. (b) CPO. For each phase, CPO is expressed for the fastest, intermediate and slowest P-wave propagation axes. Phases are ranked by descending order of abundance. Axes in bold font are the main axes described in the text. (c) Calculated seismic properties (V_P, AV_P and AV_S) of the monocrystalline aggregates. Stereographic normalized plots represent the spatial distributions of V_P (top) and AV_S (bottom). (d) Calculated seismic properties of the whole rock aggregate.

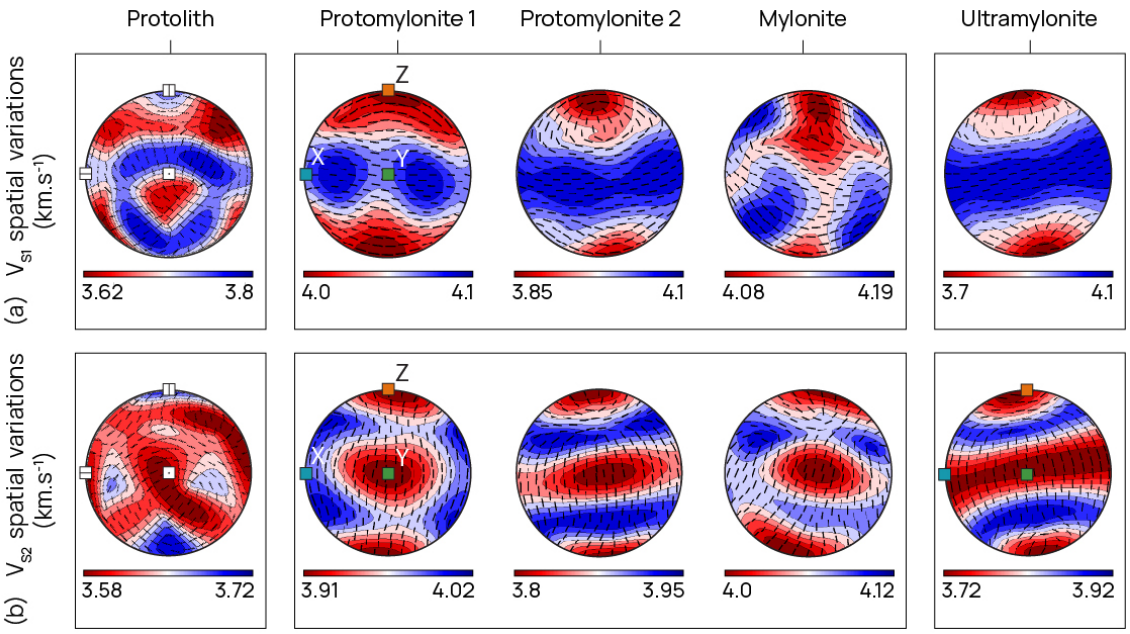

Figure 24: S6. Spatial distributions of V_{S1} and V_{S2} of the rock aggregates, calculated from petrofabrics.

S10. Bulk elastic tensors (Cij) calculated by EBSD for the samples of the strain gradient developed in the Neves metagranodiorite, and additional informations (lithology, P-T conditions, step size of EBSD measurements).

Sample	Rock type	Metamorphic grade	Location	Cij						Step size (µm)	Density	P (GPa)	T (°C)
13NEV01A	Weakly deformed metagranodiorite	Amphibolite	Zillertäl massive (Tauern Window, E. Alps)	107.45	30.87	31.63	0.03	-0.94	0.37	33.3	2.8	0.5-0.8	500-550
				30.87	105.65	30.63	0.49	-0.28	0.08				
				31.62	30.63	105.59	-2.41	-2.2	0.54				
				0.03	0.49	-2.41	35.88	0.97	0.16				
				-0.94	-0.28	-2.2	0.97	36.49	0.03				
				0.37	0.08	0.56	0.16	0.03	35.63				
18NEV01A	Protomylonite 1			129.74	32.74	32.28	0.42	-0.08	0.55	10.6			
				32.74	117.15	32.03	-0.22	-0.19	0.26				
				32.28	32.03	124.17	-0.26	0.39	-0.14				
				0.42	-0.22	-0.26	42.81	0.41	0.06				
				-0.08	-0.19	0.39	0.41	46.66	0.22				
				0.55	0.26	-0.14	0.06	0.22	44.65				
18NEV01B	Protomylonite 2			128.27	31.97	32.95	0.09	0.63	1.5	12.4			
				31.97	114.32	31.25	1.21	0.18	-0.02				
				32.95	31.25	123.93	1.92	0.18	0.46				
				0.09	1.21	1.92	40.37	0.6	0.22				
				0.63	0.18	0.18	0.6	46.1	1.21				
				1.5	-0.02	0.46	0.22	1.21	42.13				
13NEV01C	Mylonite			133.47	32.6	33.77	0.15	1.33	-1.21	10.1			
				32.6	127.44	33.16	1.16	-0.04	-0.59				
				33.77	33.16	126.84	0.72	0.6	-0.24				
				0.15	1.16	0.72	45.15	-0.72	0.4				
				1.33	-0.04	0.6	-0.72	47.7	0.7				
				-1.21	-0.59	-0.24	0.4	0.7	46.89				
13NEV01D	Ultramylonite	Upper Greenschist		120.14	24.35	27.07	-0.1	0.42	3.27	10.6			450-500
				24.35	99.81	23.59	1.36	-0.17	0.46				
				27.07	23.59	121.08	0.15	0.04	0.56				
				-0.1	1.36	0.15	39.14	1.28	-0.01				
				0.42	-0.17	0.04	1.28	46.91	0.5				
				3.27	0.46	0.56	-0.01	0.5	39.48				

S10 (continued). Numer of points indexed by EBSD (N) and modal proportions of each phase used in tensor calculation. N.B. : modal proportions are estimated by combining EBSD reports, X-ray mapping, cathodoluminescence imaging, since the number of points indexed by EBSD is often underestimated, especially for phyllosilicates.

Sample	Albite		Biotite		Epidote		Garnet		Jadeite		K-feldspar		Oligoclase		Quartz		White mica	
	N	Mode (%)	N	Mode (%)	N	Mode (%)	N	Mode (%)	N	Mode (%)	N	Mode (%)	N	Mode (%)	N	Mode (%)	N	Mode (%)
13NEV01A	-	-	20172	14	1754	1	-	-	-	-	39678	9	228510	48	106303	28	-	-
18NEV01A	-	-	22295	14	20351	4	8545	2	-	-	10252	2	255666	45	160318	29	8111	5
18NEV01B	-	-	14934	13	38519	4	3947	1	-	-	26964	3	485499	48	256484	26	8177	5
13NEV01C	-	-	265517	9	30889	7	7521	2	-	-	18389	3	265517	46	113642	33	5851	4
13NEV01D	72977	12	-	-	-	-	-	-	-	-	9530	3	72977	18	171902	43	6302	21